Marine Chemistry 246 (2022) 104161

Contents lists available at ScienceDirect

Marine Chemistry

journal homepage: www.elsevier.com/locate/marchem

The role of the Dotson Ice Shelf and Circumpolar Deep Water as driver and source of dissolved and particulate iron and manganese in the Amundsen Sea polynya, Southern Ocean

Mathijs van Manen [a], Shigeru Aoki [c], Corina P.D. Brussaard [b,d], Tim M. Conway [e], Charlotte Eich [b,d], Loes J.A. Gerringa [a], Jinyoung Jung [f], Tae-Wan Kim [f], SangHoon Lee [f], Youngju Lee [f], Gert-Jan Reichart [a,g], Hung-An Tian [a], Flora Wille [a], Rob Middag [a,h,*]

[a] NIOZ Royal Netherlands Institute for Sea Research, Department of Ocean Systems, PO Box 59, 1790 AB Den Burg, the Netherlands
[b] NIOZ Royal Netherlands Institute for Sea Research, Department of Marine Microbiology & Biogeochemistry, PO Box 59, 1790 AB Den Burg, the Netherlands
[c] Institute of Low Temperature Science, Hokkaido University, Sapporo 060-0819, Japan
[d] Institute for Biodiversity and Ecosystem Dynamics (IBED), University of Amsterdam, 1098 XH Amsterdam, the Netherlands
[e] College of Marine Science, University of South Florida, St Petersburg, FL 33701, USA
[f] Korea Polar Research Institute, 26, Songdomirae-ro, Yeonsu-gu, Incheon 21990, Republic of Korea
[g] Department of Earth Sciences, Faculty of Geosciences, Utrecht University, Utrecht, the Netherlands
[h] Centre for Isotope Research - Oceans, University of Groningen, PO Box 72, 9700 AB Groningen, the Netherlands

ARTICLE INFO

Keywords:
GEOTRACES
Trace metal
Southern Ocean
Iron limitation
Biogeochemistry

ABSTRACT

Coastal areas around Antarctica such as the Amundsen Sea are important sources of trace metals and biological hotspots, but are also experiencing the effects of climate change, including the rapid thinning of ice sheets. In the central Amundsen Sea Polynya (ASP), both bio-essential dissolved Fe (DFe) and dissolved Mn (DMn) were found to be depleted at the surface, indicating substantial biological uptake and/or precipitation. Close to the Dotson Ice Shelf (DIS) there were elevated surface concentrations of DMn (>3 nM) but surprisingly not for DFe (<0.3 nM). While Fe-binding ligand data suggests that ligands were abundant near the DIS, these were most likely not strong enough to outcompete scavenging and thus increase DFe substantially in the outflow. In contrast to the dissolved phase, particulate Fe (PFe) and Mn (PMn) concentrations (both labile and refractory fractions) were elevated over the entire water column close to the DIS and partly in the central ASP. We hypothesize that DFe was released from the DIS and immediately established an equilibrium with the labile particulate Fe (L-PFe)pool, via (reversible) scavenging, as indicated by a positive correlation between L-PFe and DFe in the outflow. This scavenging results in relatively low DFe concentrations, but the pool of labile PFe likely buffers the DFe pool when DFe is decreasing, e.g. due to uptake by phytoplankton. The DFe distribution also shows that inflowing modified circumpolar deep water (mCDW) and benthic sediments are clear and important sources for both DFe and DMn in the ASP. Refractory Fe and Mn likely have a lithogenic source, whereas the labile fractions are mostly biogenic in surface waters, and authigenic in deep waters (>100 m depth). We compared different uptake ratios, underlining that uptake ratio estimates do not necessarily capture natural variability and it is likely better to use a range of values. In the future, climate change may increase the heat flux of mCDW and thereby the melting of the DIS. This will most likely cause an increased input of Fe and Mn into the ASP, which may fuel increased levels of primary productivity in the ASP.

1. Introduction

The Southern Ocean plays an important role in mediating global climate (Rintoul, 2018). The global ocean has taken up between 25 and 30% of anthropogenic CO_2 that was released into the atmosphere (Khatiwala et al., 2009), with about 40% of this uptake occurring in the Southern Ocean (Frölicher et al., 2015). The atmospheric CO_2 concentrations would be approximately 50% higher than they are today when

* Corresponding author.
E-mail address: rob.middag@nioz.nl (R. Middag).

https://doi.org/10.1016/j.marchem.2022.104161
Received 2 January 2022; Received in revised form 22 July 2022; Accepted 15 August 2022
Available online 19 August 2022

this global uptake would not be in place (Raven and Falkowski, 1999) In the Southern Ocean, typically large phytoplankton productivity occurs, known as phytoplankton blooms, notably in coastal Antarctic waters and such blooms contribute to the sequestering of CO_2. One of these coastal regions in the Southern Ocean with high productivity is the Amundsen Sea (Arrigo and Van Dijken, 2003), located between 100° and 135°W, south of 71°S, along the margin of the Marie Byrd Land sector of the West Antarctic Ice Sheet (Nitsche et al., 2007). There are two polynyas in the Amundsen Sea, the Amundsen Sea Polynya (ASP) and the Pine Island Glacier Polynya (PIG), from which the ASP is the largest (27,333km^2). Polynyas are reoccurring areas of seasonally open water surrounded by sea ice, and dominate the energy and material transfer between the atmosphere and ocean in coastal Antarctica. Polynyas are often highly biologically active since they are the first open water areas to be exposed to the increasing solar irradiance during springtime and are often located near trace metal sources (Arrigo and Van Dijken, 2003; Arrigo and van Dijken, 2015). There should be sufficient nutrients and light available to sustain these larger phytoplankton blooms in the ASP (Alderkamp et al., 2013; Kwon et al., 2021; Oliver et al., 2019; Park et al., 2017) (Wu et al., 2019) (Pausch et al., 2019). The trace metal iron (Fe) and possibly manganese (Mn) are known to limit primary productivity in the Southern Ocean (Brand et al., 1983; Browning et al., 2021; Peers and Price, 2004). Both trace elements serve as micronutrients for all living organisms and are required for many cellular processes, including phytoplankton carbon and nitrogen fixation, nitrate and nitrite reduction, chlorophyll synthesis and the electron transport chains of respiration and photosynthesis (Twining and Baines, 2013). Mn is most notably needed in Photosystem II, for the splitting of water by photoautotrophs to supply electrons to the reaction center of PS II (Raven, 2013; W. G. Sunda et al., 1983).

Recent modelling studies suggest that ice sheet melt plays an important role in supplying Fe to the ASP (St-Laurent et al., 2017, 2019). Furthermore, Sherrell et al. (2015) studied the distribution and dynamics of DFe and other bioactive trace metals (Mn, Ni, Cu and Zn) in the ASP and they suggested that the accelerated basal melt of the ice shelves in the ASP, caused by the inflow of warm circumpolar deep water (CDW) underneath the ice shelves, plays a critical role in providing the Fe flux needed to maintain the intense phytoplankton bloom in the ASP. Additionally, organic Fe-binding ligands, which complex >99% of dissolved Fe are likely an important factor in the bioavailability and biogeochemical cycling of Fe (Gledhill and Buck, 2012). Earlier work in the Amundsen Sea indicated that iron-binding ligands were nearly saturated at locations near the glaciers. Important sources are thought to be the melting glaciers and the CDW (Thuróczy et al., 2012).

When it comes to trace metals, studies often take only the dissolved phases (<0.2 μM) into account as they are believed to be bioavailable (Shaked and Lis, 2012). However, over the past years it becomes increasingly clear that the particulate phase of Fe and Mn can also play an important role in the delivery of bioavailable trace metals to the water column (Boyd et al., 2017; Laglera et al., 2017). Particulate trace metals often exceed dissolved concentrations and likely are part of, and a source to, the bioavailable trace metal pool (Fitzsimmons et al., 2017; Gerringa et al., 2012; Gerringa et al., 2020; Hurst et al., 2010; Milne et al., 2017). Particulate trace metals are associated with suspended particulate matter such as phytoplankton cells, detrital particles, authigenic minerals, lithogenic minerals and suspended sediments (Chester and Hughes, 1967; Cullen and Sherrell, 1999; Fitzsimmons et al., 2017). Importantly, particles can be both sources and sinks for dissolved trace metals by processes such as (ligand mediated) dissolution, remineralization, scavenging and biological uptake and therefore play an important role in trace metal cycling (Goldberg, 1954; Turekian, 1977). To date, only Planquette et al. (2013) have focused on particulate trace metals in the Amundsen Sea, with a primary focus on Fe in the Eastern Amundsen Sea and the Pine Island Polynya (PIP) area, and showed that the influence of lithogenic particles in the water column dominated. Additionally, the elemental composition and spatial distribution of the particulate trace metals suggested that sediment resuspension and ice shelf melt mainly govern the supply of particulate Fe to the Amundsen Sea and that these sources potentially can support the phytoplankton bloom in the ASP (Planquette et al., 2013).

Overall, there is limited insight based on the combination of both dissolved and particulate distributions of Fe and Mn in the ASP. This study aims to give new insights in the fate of Fe and Mn, both now as well as in the future. This study reports the concentrations of both dissolved (<0.2 μm) and particulate (>0.45 μm) Fe and Mn fractions in the ASP, whereas most of the previously available data on Fe and Mn in the ASP are for DFe and DMn (Gerringa et al., 2012; Sherrell et al., 2015). To further unravel the dynamics of dissolved and particulate Fe and Mn, in this important region, in the current study particulate Fe (PFe) and Mn (PMn) were studied using a sequential leaching approach to assess the potential biogenic and lithogenic fractions.

2. Materials and methods

2.1. Sample collection and analysis

Samples were collected onboard the South Korean icebreaker RV Araon during the ANA08B research expedition to the Amundsen Sea in the austral summer of 2017/2018. The sampling period spanned from the 24th of January to the 2nd of February 2018. A total of 10 full depth stations were investigated with a maximum of 12 sampling depths. The transect followed the in- and outflow of CDW in the ASP through a trough near the Dotson ice shelf. The ASP was surrounded by sea ice at the start of the sampling campaign, whereas the polynya had started to open to the open ocean on the northwest side by the end of sampling (Fig. 1). Along this transect, station 53 was located off the shelf and outside the polynya in the marginal sea ice zone, station 52 was located in the sea ice zone next to the polynya at the shelf break, stations 42 and 36 were located at the Dotson Ice Shelf front on the in -and outflow side respectively, and the remaining stations were located in the central open water body of the ASP (Fig. 2).

Water was collected with the 'Titan' ultraclean CTD sampling system for trace metals (De Baar et al., 2008) mounted with pristine large volume samplers (Rijkenberg et al., 2015). To prevent light shock of phytoplankton, the original PVDF samplers were replaced by a light-proof version of the Pristine samplers and were made from polypropylene. The salinity (conductivity), temperature, fluorescence, depth (pressure) and oxygen were measured with a CTD (Seabird SBE 911+) mounted on the trace metal clean sampling system of NIOZ (De Baar et al., 2008). The sampling system was deployed on a 11 mm Dyneema cable without internal conductive wires and therefore an SBE 17 plus V2 Searam in a titanium housing provided power, saved the CTD data and closed the sampling bottles at pre-programmed depths. After deployment, the complete CTD sampling system was placed in a cleanroom environment inside a modified high cube shipping container and subsamples were collected. The water for dissolved trace metal and iron-binding ligand analysis was filtered from the samplers over a 0.2 μm filter cartridge (Sartobran-300, Sartorius) under pressure (0.5 bar overpressure) of (inline pre-filtered) nitrogen gas, whereas for the samples for nutrients and particulate trace metals no filter cartridge was used. Subsamples for dissolved trace metal analysis were collected in acid cleaned, Low-density polyethylene (LDPE), bottles following GEOTRACES protocols (Cutter et al., 2017). Sample bottles (125 mL) were filled after five rinses with the sampled seawater. These seawater samples were acidified by adding ultra-pure hydrochloric acid (HCl; Baseline®HCl (Seastar Chemicals Inc), resulting in a concentration of 0.024 M which leads to a pH of ~1.8 with. For iron-binding ligands, samples were taken in HCl cleaned LDPE bottles and were stored right after, without acidification, at −20 °C until further analysis.

For particulate trace metals, unfiltered samples were collected in 10 L acid cleaned carboys (VWR Collection) and stored in dark plastic bags

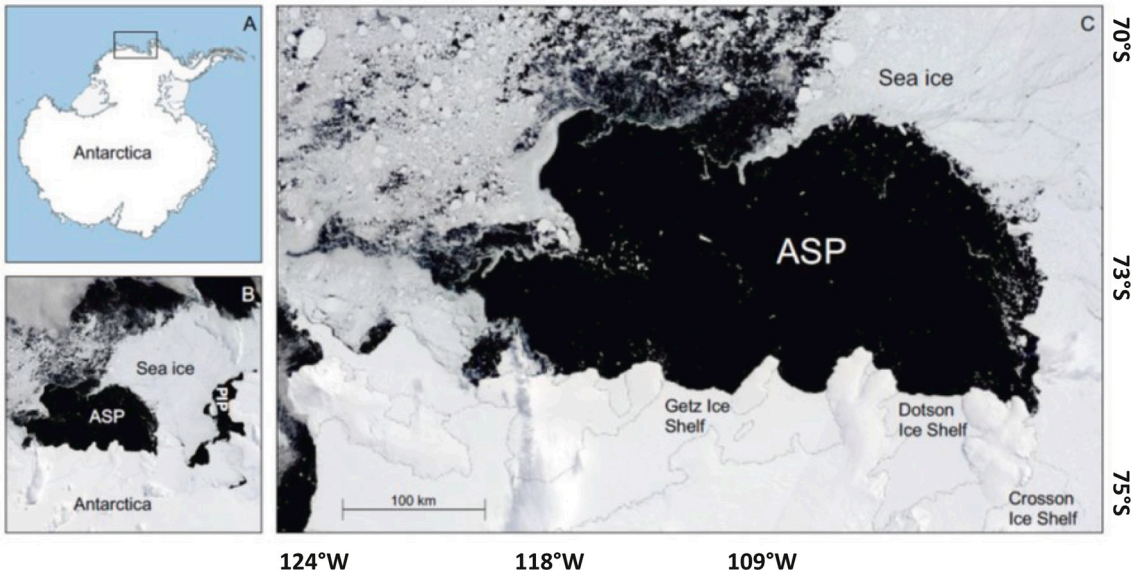

Fig. 1. A Location of the Amundsen Sea in Antarctica; B Amundsen Sea with the locations of the Amundsen Sea Polynya (ASP) C ASP with the Crosson, Dotson and Getz Ice Shelves; (B-C) Moderate Resolution Imaging Spectroradiometer (Terra/MODIS) true color satellite images from January 10, 2018 (source: NASA Worldview).

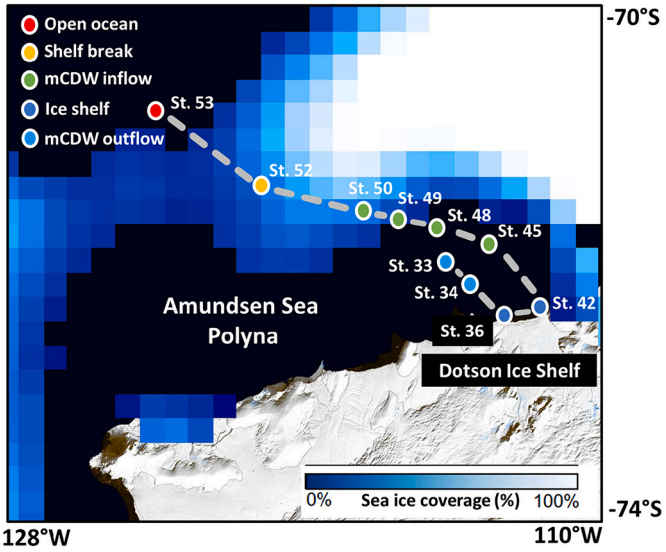

Fig. 2. Map of the study area with the cruise transect (gray dashed line), trace metal sampled stations (colored dots) and approximate outline with use of percentage sea ice coverage at the end of sampling (30th January 2018); 12 km spatial resolution Advanced Microwave Scanning Radiometer- E/Advanced Microwave Scanning Radiometer-2 (AMSR-E/AMSR2) images (source: NASA Worldview).

close to the ambient seawater temperature until the moment of filtration. Carboys were rinsed five times with the sample seawater and when timing between sampling stations allowed, carboys were additionally cleaned and rinsed with HCl. Process blanks using 0.2 μm filtered seawater were sampled and analyzed during another expedition and were comparable to filter blanks (see section 2.3.3.). Before the expedition, 25 mm poly-ether-sulfone (PES) disc filters (0.45 μm PAll Supor) and polypropylene filter holders (Advantec) were cleaned by heating them at 60 °C for 24 h in 3× sub-boiled distilled 1.2 M HCl (VWR Chemicals – AnalaR NORMAPUR) and rinsing them 5 times with MQ water (18.2 MΩ) (Ohnemus et al., 2014). Filters were stored in MQ water (18.2 MΩ) until use. By using 0.45 μm filters, the results will comparable with other groups within the GEOTRACES community, but the filtrates were not collected due to time and personnel limitations. Filtrations were started within a maximum of two hours after sampling (GEOTRACES 2010). Before the start of the filtrations, samples were gently homogenized and the PES filters were placed on the filter holders. Filter holders were placed on the caps (Nalgene) of the carboys using polypropylene luer-locks (Cole-Palmer). Carboys were then hung upside down onto the CTD frame using a custom-made polypropylene carboy frame. Filtration was done under nitrogen gas pressure (0.3 bar overpressure). Samples were filtered for a maximum of two hours and checked regularly for leaks. After filtration, excess seawater on top of the filters was removed by gentle air pressure. The filters were removed from the filter holders and were folded in half, placed in a small plastic bag and stored frozen (−20 °C) until analysis. Water samples for $\delta^{18}O$ were drawn from Niskin bottles of a regular CTD rosette, stations were similar but cast was different from trace metal samples.

2.2. Dissolved trace metal processing

Dissolved trace metal samples were preconcentrated using a SeaFAST pre-concentration system (ESI) followed by ICP-MS analysis (Section 2.3.5) following Gerringa et al. (2020). Briefly, a Nobias PA1 resin was used in the pre-concentration column and before introducing the samples into the SeaFAST system, 30 mL sample was pipetted into an acid-cleaned FEP vial. Peroxide (final concentration 10 μM) and an indium/lutetium internal standard at a final concentration of respectively 3.3 and 1.5 nM were added before UV digestion (after Middag et al., 2015)). All actions were conducted in a laminar flow cabinet (ISO class 5), The samples were UV-digested for 4 h in a custom-made UV box. After digestion the samples were pre-concentrated with the SeaFAST system using two loops of 10 mL and were eluted into 350 μL elution acid (1.5 M Teflon distilled HNO_3 with rhodium as internal standard) which gives a pre-concentration factor of 57.14.

The dissolved trace metal concentrations were calibrated via standard additions using a mixed stock solution made of 1000 ppm single spike standards. A typical calibration line consisted of seven standard additions where the maximum standard additions are comparable to maximum concentrations in the marine environment. The recovery was verified in each analytical run by comparing the slope of the seawater calibration curve (multi-element standard added to seawater) and the

eluent calibration curve (multi-element standard added directly to the elution acid) after Biller and Bruland (2012). Blank contributions (Table 1) from sample handling, pre-concentration, and analytical steps were determined by analyzing acidified MQ water (~1.8 pH) as a sample and exposing the sample to the same procedure as the samples. The accuracy and precision of the measurements were determined by measuring GEOTRACES community consensus reference materials SAFE D1 and S and GSC and GSP as well as in-house reference seawater samples (Table 2).

2.3. Particulate filter sample processing

The particulate trace metal (and phosphorus) PES filters were treated with two successive digestion protocols to determine the labile and refractory fraction. All vials that were used in the digestion procedures were rigorously cleaned with HF and HCl beforehand. Vial blanks were checked before the start of each batch of measurements. Before and between use vials were rinsed 5 times with MQ water (18.2 MΩ), refluxed in 3× sub-boiled distilled 7 M HCl (VWR Chemicals – AnalaR NORMAPUR®) at 110 °C on a hotplate for a minimum of 12 h, and rinsed 5 times with MQ again before use. All actions were conducted in a laminar flow cabinet (ISO class 5), except for refluxing, drying and all steps involving HF, which were done in a regular fume hood equipped with a heating block (Analab). Drying steps were performed in a closed environment (Analab) and refluxing was done in closed vials to prevent atmospheric exchange. Both the laminar flow cabinet and fume hood were located in a clean lab (ISO class 8).

2.3.1. Labile particulate fraction

To solubilize the labile fraction (indicated by L) of the particulate trace metal samples, the filters were subjected to a leach initially developed by Chester and Hughes (1967), further modified and developed by Berger et al. (2008) and evaluated by Twining et al. (2015). Filters were placed in cleaned 2 mL vials by unfolding them against the wall of the vial (Eppendorf) with tweezers, to which a solution of 1.8 mL of 4.35 M (25%) 2× sub-boiled distilled acetic acid and 0.02 M (2%) hydroxylamine hydrochloride (Sigma-Aldrich – 99.999% trace metal basis) was added. The vials were heated to 95 °C for 10 min in a water bath and were subsequently cooled down to room temperature. After being in contact with the leach solution for a total of 2 h, the filters were moved to a 30 mL Teflon vial (Savillex) and processed for refractory elements. The remaining leachate was centrifuged at 16,000 RCF for 10 min to bring any remaining particles to the bottom of the solution in the vials. Next, 1.6 mL of leachate was transferred to a separate 30 mL Teflon vial (Savillex) and 100 μL of concentrated HNO_3 was added. The vials were then heated to dryness at 110 °C. The dried vial contents were re-dissolved in 2 mL 1.5%, 3× sub-boiled distilled HNO_3 (10 ng mL-1 Rh internal standard), refluxed at 110 °C for 30 min and transferred to 2 mL Cryovials® for storage and subsequent analysis. These samples represent the labile fraction.

2.3.2. Refractory particulate fraction

Refractory elements were digested following a total digestion protocol developed by Cullen and Sherrell (1999) and further modified by Planquette and Sherrell (2012). The remaining 0.2 mL of leachate and particles in the labile leach vial from the previous step was transferred to the Teflon vial already containing the filters. Final samples were corrected for the 0.2 mL labile leachate. After transferring the leachate, 2 mL of a solution of 3× sub-boiled distilled 8.0 M (50%) HNO3 (VWR Chemicals – AnalaR NORMAPUR) and 2.9 M (10%) HF (Merck - Supelco) was added. The vials were closed tightly and refluxed for 4 h at 110 °C. The filters did not remain adhered to the walls of the vials and were visibly altered by digestion, but still intact. Afterward, the vials were cooled, and the contents were poured into secondary Teflon vials (Savillex) without transferring the filters. The original digestion vials were thoroughly rinsed with MQ water (18.2 MΩ) to ensure the complete transfer of the sample. This was also poured into the secondary Teflon vials and the filters were discarded. The secondary Teflon vials were then heated to dryness at 110 °C. To the dried vial contents, 1 mL of a solution of 8.0 M (50%) 3× sub-boiled distilled HNO_3 (VWR Chemicals – AnalaR NORMAPUR) and 15% H_2O_2 (Merck – Suprapur) was added. The vials were refluxed for 1 h at 110 °C and subsequently cooled to room temperature. Adding reagents and refluxing were repeated once, after which the vials were heated to dryness at 110 °C. The samples were redissolved in 2 mL 1.5% 3× sub-boiled distilled HNO_3 with 10 ppb Rh as internal standard and transferred to 2 mL Cryovials® for storage and analysis. These samples represent the refractory fraction, the results are denoted by R.

Table 1
Blanks and limit of detection (LOD) defined as three times the standard deviation of the blank.

	MQ blank	LOD
Fe ($n = 20$)	35.0 pM ± 17 pM	51.9 pM
Mn (n = 20)	1.0 nM ± 0.9 nM	2.7 pM

Table 2
GEOTRACES community consensus reference materials SAFE D1 and S and GSC and GSP. Values are all in nmol-1 l.

	Mn	Fe
GSP ($n = 3$)	0.73 nM ± 0.01 nM	0.13 nM ± 0.01 nM
Certified value	*0.78 nM ± 0.03 nM*	*0.16 nM ± 0.05 nM*
GSC (n = 3)	2.03 nM ± 0.04 nM	1.42 nM ± 0.02 nM
Certified value	*2.18 nM ± 0.08 nM*	*1.53 nM ± 0.12 nM*
S (n = 3)	0.98 nM ± 0.02 nM	0.1 nM ± 0.001 nM
Certified value	*0.81 nM ± 0.06 nM*	*0.095 nM ± 0.009 nM*
D1 (n = 3)	0.43 nM ± 0.005 nM	0.74 nM ± 0.002 nM
Certified value	*NA*	0.69 nM ± 0.04 nM

2.3.3. Blanks

Two types of blanks were analyzed to determine the average background trace metal concentration of the different components in the digestion procedure; acid blanks and filter blanks (Table 3). Reagent blanks simply consisted of the digestion acids. These acid blanks were treated identically to the particulate trace metal samples, except for the steps involving filter handling and the removing of the filter from the filter holders. Therefore, the vial blank is included in this reagent blank. Filter blanks consisted of new acid cleaned PES disc filters that had not been in contact with seawater. Filters were placed in the Eppendorf tube and were treated and analyzed identically to the particulate trace metal filters. All blanks were corrected for outliers by omitting values that did not fall within ±2SD of the blank average (Table 3).

2.3.4. Certified reference materials

Accuracy and precision of the digestions were assessed by Certified Reference Materials (CRMs). There is no available CRM for marine

Table 3
Acid and filters (pmol/vial) of the labile leach (labile) and subsequent total digestion (refractory).

	Al	P	Mn	Fe
Acid blank Labile	288.9	55.9	1.0	42.7
± 1SD	210.4	26.8	0.5	26.4
Acid blank Refractory	205.5	79.4	0.3	15.9
± 1SD	33.3	21.9	0.2	9.4
Filter blank Labile	358.6	93.3	1.4	42.5
± 1SD	146.0	81.0	0.3	9.6
Filter blank Refractory	302.7	74.1	0.7	33.1
± 1SD	111.3	19.3	0.2	9.0

Please note the refractory blank was assessed sequentially after the labile leach, i.e. the total blank is the sum of the labile and refractory contribution.

suspended particulate matter, therefore accuracy could only be approximated by analysis of other available CRMs. For this study BCR-414 (freshwater phytoplankton, certified by the Community Bureau of Reference, European Commission's Joint Research Centre), PACS-2 and MESS-3 (marine sediments, National Research Council of Canada) were analyzed. For each CRM, 10–30 mg was digested. The recommended sample weights are however 100 mg for BCR-414 and 250 mg for PACS-2 and MESS-3. The lower sample weights in this study were chosen to be representative of actual marine particulate suspended matter concentrations (similar to Ohnemus et al., 2014). BCR-414 was subjected to the consecutive labile leach and refractory total digestion and separately to the total digestion. PACS-2 and MESS-3 were only subjected to the total digestion (Table 4). In general recoveries were within the range of the CRM with lowest recovery measured for BCR-414 Mn (89% ± 3%) and highest for PACS-2 PAl (113% ± 11%).

2.3.5. ICP-MS analysis

As for dissolved samples (Section 2.2), trace metals from both particulate sample types, blanks and CRMs were analyzed by ICP-MS at NIOZ, with analysis following Gerringa et al. (2020). Rhodium was used as an internal standard and drift standards were measured after every block of 13 samples to correct for drift during the runs. Final particulate trace metal concentrations were calculated from Rh-normalized and, when needed, drift corrected values.

2.4. Dissolved nutrient analysis

Macro-nutrient analysis was performed on board as described in (Jeon et al., 2021). In short the inorganic nutrients phosphate (PO_4) and silicic acid ($Si(OH)_4$), were measured using a four-channel Auto-Analyzer (QuAAtro, Seal Analytical, Germany), according to the Joint Global Ocean Flux Study (JGOFS) protocols described by (Gordon et al., 1993).The precisions for the PO_4 and $Si(OH)_4$ measurements were ± 0.02 and ± 0.28 μmol kg respectively. NO_2 + NO_3 and NH_4 were analyzed but not shown here due to onboard contamination.

Table 4
Concentrations (μg/g; g/100 g) and recoveries (%) of Certified Reference Materials ±1SD.

	Al[g/100 g]	P[g/100 g]	Mn[μg/g]	Fe[g/100 g]
BCR-414 Certified value	N/A	N/A	299 ± 13	1.85 ± 0.19[a,b]
Combined	–	–	258 ± 5	1.78 ± 0.043[b]
Recovery (%)	–	–	86 ± 2	96 ± 2
Total digest	–	–	267 ± 8	1.89 ± 0.049[b]
Recovery (%)	–	–	89 ± 3	102 ± 3
MESS-3 Certified value	8.59 ± 0.23	0.12[a]	324 ± 1	4.34 ± 0.11
Total digest	8.75 ± 1.16	0.11 ± 0.01	302 ± 34	3.96 ± 0.51
Recovery (%)	102 ± 13	89 ± 10	93 ± 11	91 ± 12
PACS-2 Certified value	6.62 ± 0.32	0.096 ± 0.004	440 ± 19	4.09 ± 0.06
Total digest	7.45 ± 0.73	0.097 ± 0.010	442 ± 48	4.26 ± 0.46
Recovery (%)	113 ± 11	101 ± 10	101 ± 11	104 ± 11

BCR-414 was analyzed for the consecutive labile leach and total digestion (combined) and separate total digestion (total digest). MESS-3 and PACS-2 were solely subjected to the total digestion (total digest). Values are averages of triplicate samples.

[a] Only indicative value available.

[b] Concentrations in μg/g.

2.5. Iron-binding ligands

Iron-binding ligands were sampled and analyzed at five stations (st 34, 36, 42, 45 and 49). Right before analysis, samples were thawed in the dark and vigorously shaken prior to further treatment. Electrochemical analysis CLEAdCSV with salicylaldox''me (SA) as a competing added ligand (Abualhaija and van den Berg, 2014) was used. The application followed Abualhaija and Van den Berg (2014) using Metrohm equipment with Nova 1.9 (Metrohm Autolab B.V.) as the software user-interface. The conditional stability constant of SA (log *KFe'(SA) cond* = 5.9) used in this study is based on the calibration of SA against diethylenetriaminepentaacetic acid by Gerringa et al. (2021). Calculation of the ligand concentration, expressed as nanomole equivalents of Fe (nM Eq Fe), and conditional binding strength of the Fe-ligand complex was done using the nonlinear Langmuir isotherm (Gerringa et al., 2014). Free Fe, not bound by organic ligands, is calculated as described in Gerringa et al. (2014)

For the titration, 10 mL sample aliquots were added to 12 preconditioned Teflon (Fluorinated Ethylene propylene (FEP), Savillex) vials and buffered to seawater a pH of 8.2 with 0.1 M ammonium-borate buffer. Before analysis, the Teflon vials for titration were preconditioned at least three times with seawater containing SA and the intended Fe addition. For each titration point, duplicate scans were done in the same Teflon vial as voltammetric cell. Samples were purged with air (60 s) before analysis since the Metrohm system was modified to allow for air purging whilst the mercury drop formation was still executed under nitrogen pressure. Nitrogen did not leak into the space overlying the sample during the measurements in the Metrohm stand. The inorganic Fe side reaction coefficient (α_{Fe}) for pH = 8.2 was calculated using Visual MINTEQ software version 3.0 (Gustafsson, 2012) as log $\alpha_{Fe'} = 10.4$. The sample aliquots were titrated with Fe from 0 to 10 nM (with a 0.5 nM interval from 0 to 3 nM and with a 2 nM interval from 4 to 10 nM Fe (0, 0.3, 0.6, 1, 1.5, 2, 2.5, 3, 4, 6, 8, 10) and vials without Fe addition and the highest addition were prepared twice. Then, the competing ligand, SA, was added at a final concentration of 5 μM. The mixture was left to equilibrate for at least 8 h or typically overnight (Abualhaija and van den Berg, 2014).

2.6. Dissolved oxygen isotope ratio analysis

The stable oxygen isotope ratio of a water sample, with respect to Vienna Standard Mean Ocean Water (VSMOW), is expressed as $\delta^{18}O$, where $\delta^{18}O = \left\{ \frac{\left(\frac{^{18}O}{^{16}O}\right)_{sample}}{\left(\frac{^{18}O}{^{16}O}\right)_{vsmow}} - 1 \right\} \times 1000$ (‰). Water samples for $\delta^{18}O$ were drawn from the regular rosette (i.e. not the trace metal clean one) on the same stations, from the Niskin bottles by gravity filtration through inline pre-combusted (at 550 °C for 6 h) Whatman GF/F filters (47 mm in diameter) held in acid-cleaned (0.1 M HCl) polycarbonate 47 mm filter holders (PP-47, ADVANTEC). A 30 mL glass vial with polypropylene cap and polypropylene-coated insert was used to collect the water sample. The glass vial was sealed with a parafilm in order to prevent the entry of air and stored at 4 °C until analysis in refrigerators.

The $\delta^{18}O$ samples were processed using a Finnigan DELTA plus and Elementar Isoprime precision mass spectrometers at ILTS laboratory, Hokkaido University, Japan. The DELTA plus was coupled with an equilibration system automatically shaking for about 8 h in an 18 °C water bath to equilibrate with CO_2, while the Isoprime precision was coupled with equilibration system of metal insulator set up for about 16 h with 30 °C. The precision of the analysis was estimated to be 0.02‰ based on duplicated measurements (Nakamura et al., 2014).

The fractions were calculated using the approach described by Tian et al. (2022). In short, the $\delta^{18}O$ endmembers of different freshwater sources as previously reported for the Amundsen Sea (Randall-Goodwin et al., 2015), and later modified by (Jeon et al., 2021), were combined

with the three-endmember mass balance approach following Östlund and Hut (1984) and Meredith et al. (2013) to quantify the contribution of meteoric water, sea ice melt, and CDW.

2.7. Chlorophyll *a*

Chlorophyll ***a*** (Chl-a) concentrations were derived from pigment-based phytoplankton taxonomic composition analysis. For this, seawater samples were gently filtered through a GF/F glass fiber filter (45 mm diameter; Whatman, Cytiva, Marlborough, USA) at 1 °C, using a vacuum pump (200 mbar; Pal, Port Washington, NY, USA). Average sample volume needed to display green color on the filter was 1.7 L (0.75 to 2.7 L range). Filters were double-wrapped in aluminum foil, snap-frozen in liquid nitrogen and stored at −80 °C until analysis. Following, filters were freeze dried and pigments were dissolved in acetone (Van Leeuwe et al., 2006). A Zorbax Eclipse XDB-C8 column (3.5 μm particle size) was used for High-performance liquid chromatography (HPLC) pigment separation (Van Heukelem and Thomas, 2001) and detection was based on retention time and diode array spectroscopy at 436 nm (Waters 996).

3. Results

3.1. Hydrography

The temperature-salinity distribution (Fig. 3A) illustrates that the three typical water masses of the ASP were present at the time of sampling. At the open ocean station (st 53), the relatively warm and saline CDW ($T > 1$ °C, $S > 34.7$) comprised almost the entire water column except for the approximate upper 150 m (Fig. 3B). Intruding CDW is modified by mixing with overlying shelf waters and was present over the entire shelf up to the DIS front (st 42) and here is referred to as modified CDW (mCDW). Above the warm and saline mCDW intrusion, the colder and less-saline winter water (WW) was present at all stations ($\Theta \sim -1.7$ - -1.8 °C, SA: 34.3–34.4), except for st 53. Warm and relatively fresh Antarctic surface water (AASW) constituted the upper water layer and was present to maximum depths of approximately 100 m ($\Theta \sim$ 0.6–0.7 °C, $S_A < 33.8$). The coldest waters in the surface layer were located at the DIS front, the open ocean station (st 53) and the shelf-break station (st 52). These stations are subject to ice sheet meltwater input and sea ice melt respectively. The AASW in the polynya has a higher temperature than underlying waters as a result of warming by solar radiation. Similar to temperature, the lowest salinities in the surface layer were found at the open ocean station (st 53) due to sea ice melt. This shallow decreased salinity layer extended into the mCDW inflow stations (st. 45, 48 and 49). Salinities at the ice shelf stations (st 42 and 36) were not significantly lower than mCDW in or outflow stations, due to the mixing of meltwater with mCDW. Local mCDW inflow endmember was represented by the deep water (temperature > 0 °C) of station 45 and 48 and the local outflow endmember by station 36 at 295 m, which is consistent with the range of 200-400 m as reported earlier (Miles et al., 2016; Randall-Goodwin et al., 2015). The core of mCDW inflow was characterized close to the sea floor of the continental shelf (see section 3.1) whereas the core of mCDW outflow was defined by temperature (between 0.5 and 1.3 °C) and salinity (between 34 and 34.25 PSU). For shelf water, the endmember was initially defined based on the subsurface waters of st. 45 (72–235 m) based on temperature ($\Theta < -1.5$ °C). However, since there was intense biological activity in the surface at st. 45, resulting in high concentrations of labile particles, not only the surface, but also samples from 72 m to 136 m were excluded in this calculation. Station 48 was not included as a shelf-water endmember because of suspected influence of outflow waters (see the end of this section 4.1.4.). For clarity, stations will be discussed in five subgroups; open ocean station (st 53), shelf-break station (st 52), mCDW inflow stations (st 50, 49, 48, 45), ice shelf inflow station (st 42), ice shelf outflow station (st 36) and mCDW outflow stations (st 33, 34).

3.2. Macro nutrients

Macronutrients were not fully taken up at any location along the ASP transect. Dissolved phosphate (PO_4) concentrations (Fig. 4A) below the surface layer (upper 100 m) were constant (median of of 2.01 ± 0.28 μM), and there was no difference in PO_4 concentrations between CDW and WW. The lowest PO_4 concentrations were found in the surface of the central ASP (median of 1.75 ± 0.30 μM) and relatively high concentration were observed near the DIS and outside the polynya.

Throughout the transect, dissolved silicate (Si) concentrations (Fig. 4B) increased with depth reaching the highest concentrations in CDW below 400 m (mean > 400 m of 106 ± 4.48 μM). Higher silicate concentrations were also found >200 m at the mCDW outflow station (st

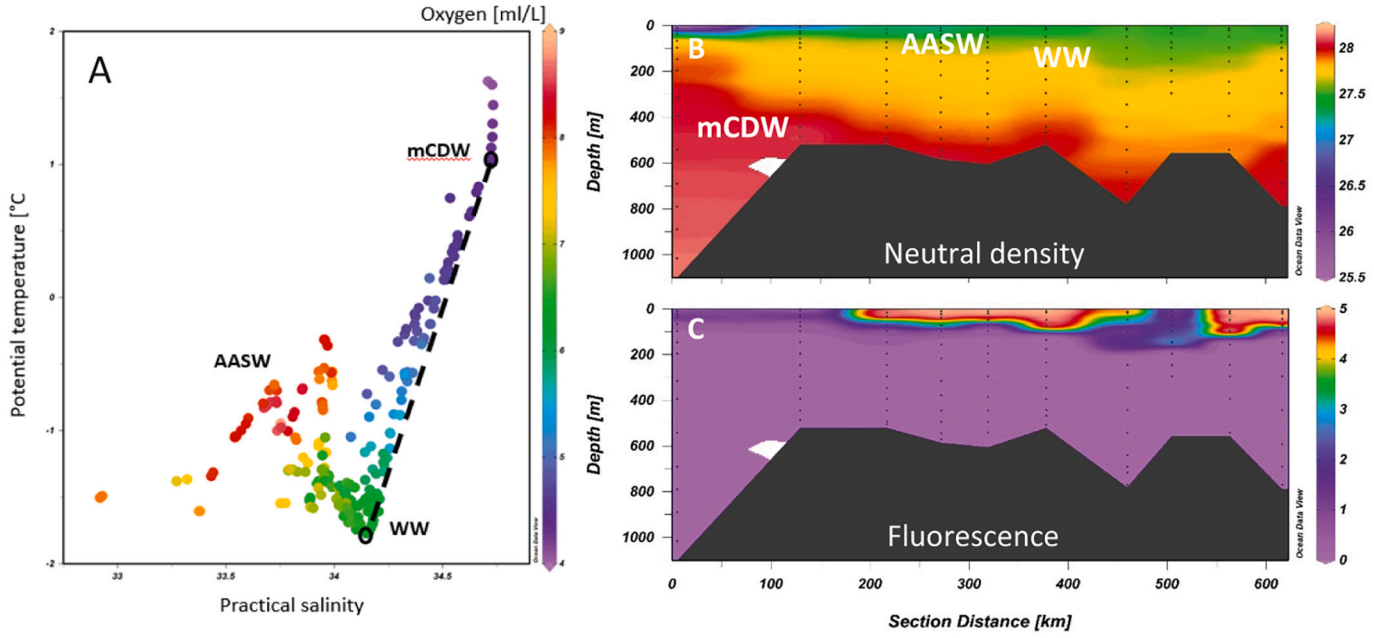

Fig. 3. A T-S plot of ASP transect and transect plots of B Neutral density (kg/M3)and C Fluorescence along the sampled transect in the ASP.

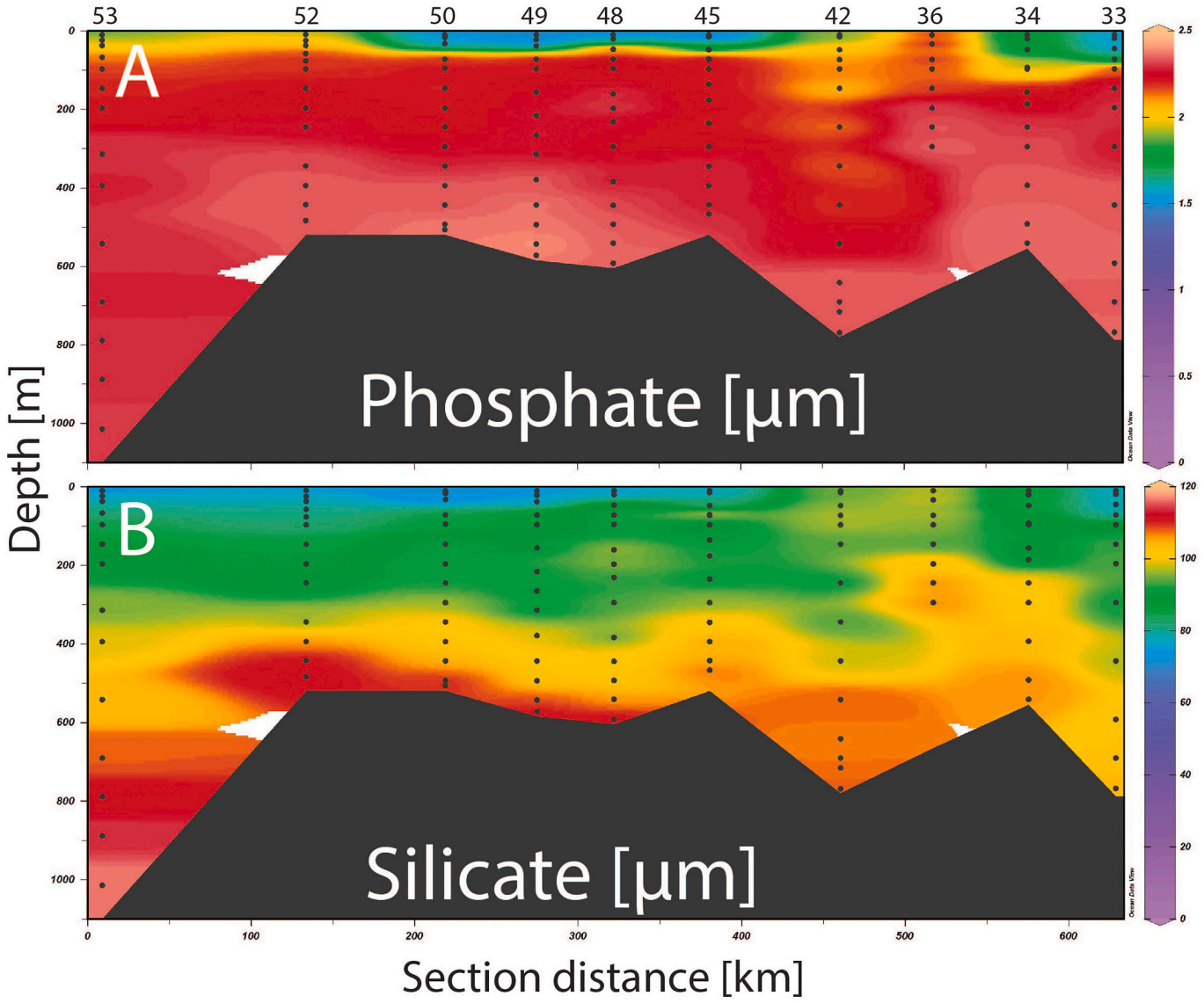

Fig. 4. Transect plots of A phosphate and B Silicate along the sampled transect in the ASP.

34) and ice shelf outflow station (st 36). The lowest Si concentrations were observed in the surface water of the central ASP (median of 82.71 ± 8.37 µM). At st 48 there was an additional sub-surface maximum of Si, around 200 m, which could be an indication of the presence of DIS outflow water.

Table 5
Total surface Chl-a concentrations (µg/m3).

Station	Chl-a
31	5.37
33	6.02
34	5.07
36	0.82
42	1.80
45	5.69
49	4.76
52	0.89
53	0.58

3.3. Chlorophyll *a*

Chlorophyll a (Chl-a) concentrations (Table 5) were highest in the central polynya stations (st 31, 33, 34, 45, 49), where concentrations ranged from 4.8 and 6.0 µg m^{-3}. This high Chl-a standing stock illustrates the presence of well-known phytoplankton bloom in the ASP (Alderkamp et al., 2015; Gerringa et al., 2012; Yager et al., 2012) during sampling. At the mCDW outflow station 36 the Chl-a concentration was lower than that at the inflow station 42 (1.8 and 0.8 µg m^{-3}, respectively). Lowest Chl-a concentrations were found for the open ocean station 53 (0.6 µg m^{-3}).

3.4. Dissolved Fe and Mn

The concentrations of DFe and DMn varied strongly with depth and location throughout the ASP (Fig. 5). In general, DFe concentrations (Fig. 5A) were lowest near the surface and increased with depth. Highest DFe concentrations (maximum 1.97 nM) were found near the sea floor and in the outflow stations. The median surface (upper 100 m depth) DFe concentration in the central ASP was low (median of = 0.19 ± 0.19 nM), consistent with previous studies for the surface ASP (Sherrell et al., 2015). The highest median concentrations were found in CDW and at the

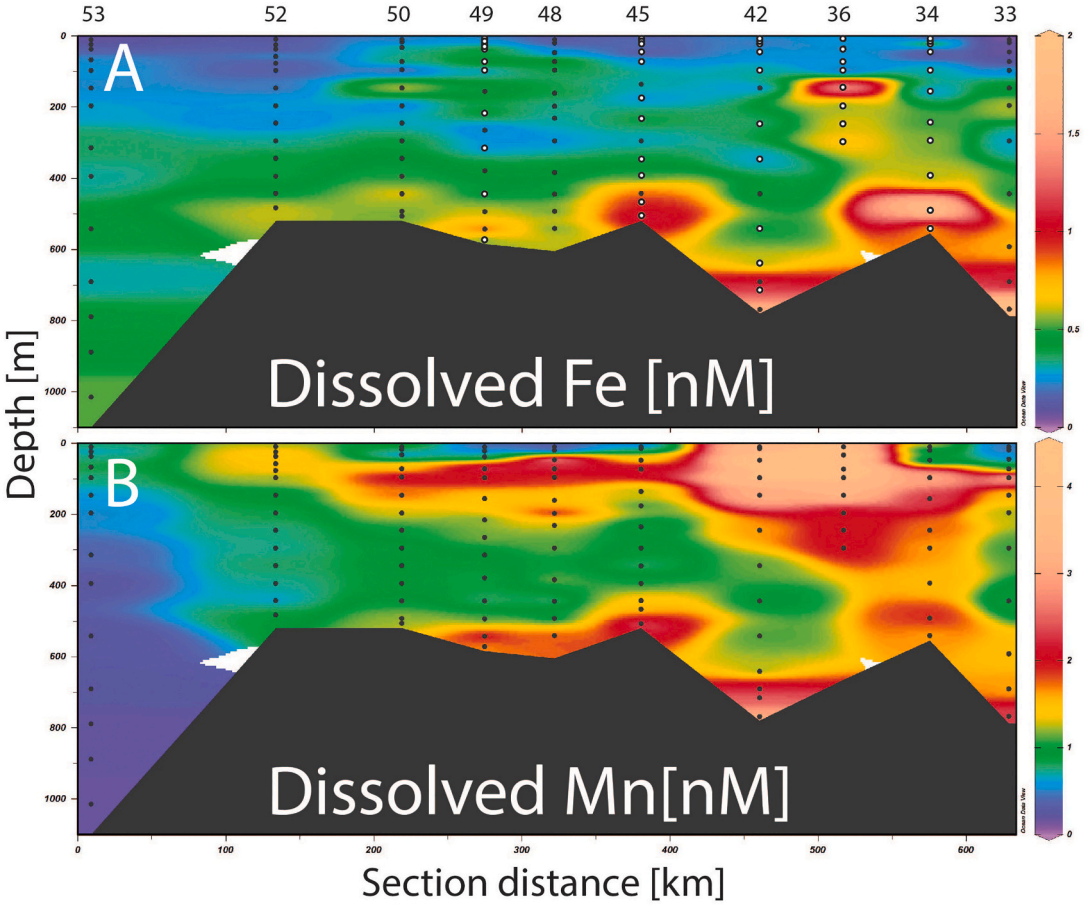

Fig. 5. Transect plots of A dissolved iron and B dissolved manganese along the sampled transect in the ASP.

outflow stations (st 33, 34, 36). There was also a subsurface maximum (~0.5 nM) observed at polynya stations (st 48, 49 and 50). This was also earlier observed in a few of the polynya stations of an earlier study (Sherrell et al., 2015).

DMn concentrations (Fig. 5B) were in relatively low near the surface, reached a sub-surface maximum and decreased with depth until an increase towards the seafloor. In the central ASP, concentrations were relatively low near the surface (median of 0.52 ± 0.64 nM) and increased at around 50 m depth in the subsurface to decrease again at >200 m depth and later increase towards the sea floor (median of 1.03 ± 0.53 nM). At the ice-shelf stations (st 36 and 42), highest DMn concentrations were found in the upper 100 m (median of 3.79 ± 0.32 nM). At the mCDW outflow station (st 34), DMn concentrations were elevated over the entire water column. Reported values are in agreement with an earlier study done in the same region (Sherrell et al., 2015).

3.5. Particulate Fe and Mn

The distribution of L-PFe (Fig. 6A) differed from the DFe distribution. The lowest concentrations were seen at the shelf break and open ocean stations (st 52 and 53). In the central ASP, surface concentrations were low (median of 1.40 ± 1.12 nM) but were higher at the ice shelf outflow station 36 (median of 6.09 ± 3.90 nM). Elevated concentrations were observed in the subsurface and deep waters of the DIS and the CDW outflow stations (st 33, 34, 36 and 42). The distribution of refractory PFe (R-PFe) (Fig. 6E) followed the same trend as L-PFe. R-PFe concentrations were, however, about 4 times higher than the L-PFe concentrations.

The highest L-PMn (Fig. 6B) concentrations were at the ice shelf outflow station 36 and in the CDW outflow in station 34. In the central ASP, surface concentrations were low (median of 1.42 ± 0.58 nM) The lowest L-PMn concentration were also seen in the open ocean station 53 (median of 0.04 nM ± 0.03 nM). In contrast to PFe, elevated concentrations were present in the entire central ASP from deeper than 200 m downwards. The distribution of R-PMn (Fig. 6F) was comparable to the L-PMn with regards to trends, but actual concentrations of R-PMn were ~ 4 times lower than L-PMn concentrations.

3.6. Particulate phosphate and aluminum

Labile and refractory particulate phosphorus (PP) distributions (Fig. 6C, G) resembled the fluorescence (Fig. 3C). Maximum concentrations were found in the upper 100 m, followed by 100-fold lower concentrations for labile PP and 10-fold lower concentrations for refractory PP deeper in the water column. In the upper 100 m, concentrations were highest at the polynya and shelf break stations (st 33, 34, 45, 48, 49 and 52) and lowest in the open ocean (st 53) and at the ice shelf stations (st 36 and 42).

Particulate aluminum (PAl) predominantly occurred in the refractory fraction, with refractory concentrations being approximately 20-fold higher than labile concentrations (Fig. 6D, H). Both labile and refractory PAl concentrations followed roughly the same distribution trends along the transect. The highest concentrations were observed at the stations closest to the ice shelf outflow station (st 36) and mCDW outflow station (st 34). At these stations, maximum concentrations were found at the same depths for both the labile and refractory fractions. PAl has a higher concentration at one of the mCDW inflow stations (st 48), with maximum concentrations at the two deepest sampled depths. The open ocean station (st 53) and shelf break station (st 52) had the lowest PAl concentrations.

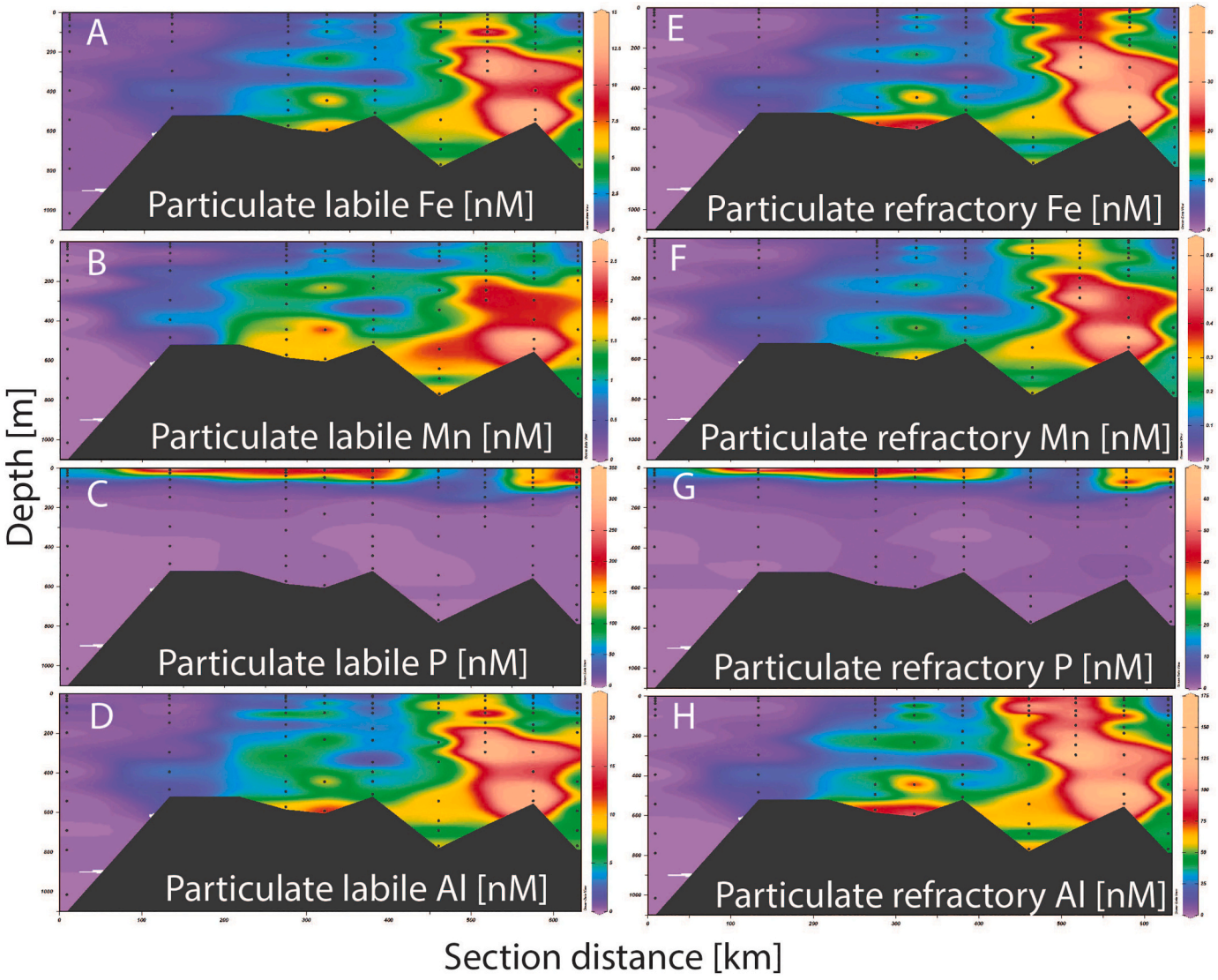

Fig. 6. Transect plots of A labile particulate iron, B manganese, C phosphate D alumnium and E refractory particulate iron, F manganese, G phosphate and H alumnium along the sampled transect in the ASP.

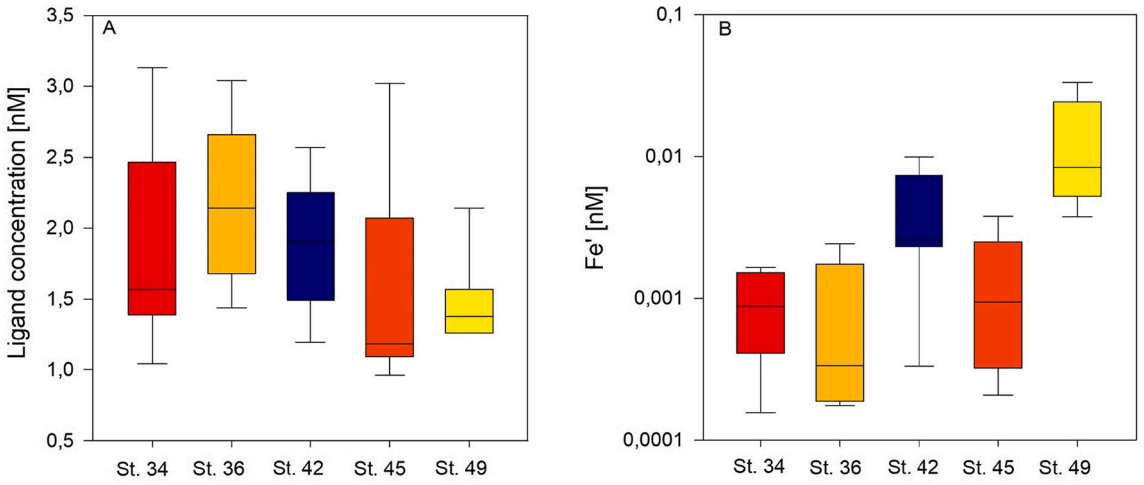

Fig. 7. A ligand concentrations per station (full water column) B Free iron concentrations in the deep (>100 m depth).

3.7. Iron-binding ligands

The total ligand concentration (Figs. 5 and 7) (average = 1.77 ± 0.59 nM Eq of Fe) had a range from 0.96 to 3.04 nM equivalent of Fe. On average, lowest concentrations were observed in the mCDW inflow station furthest away from the DIS (st 49) and highest concentrations at the ice shelf station 36. However, there was no significant difference (One-way ANOVA on ranks, $p > 0.05$) between stations (Fig. 7A). Iron-binding ligands were at all stations in excess with respect to DFe.

Lowest free-iron (Fe') concentrations (>100 m depth) were observed at the ice shelf station 36 and highest concentrations at the mCDW inflow station 49 (Fig. 7B). There was a significant difference observed between mCDW inflow station 49 and all other analyzed stations (st 34, 36, 42 and 45) (One-way ANOVA on ranks, $p < 0.05$). All data is available (https://doi.org/10.25850/nioz/7b.b.bd)

4. Discussion

4.1. Sources of dissolved and particulate Fe

The particulate trace metals were filtered over a 0.45 μm filter (as described in the GEOTRACES cookbook), whereas dissolved trace metals were filtered with a 0.2 μm filter. Due to time and personnel limitations, the filtrate was not collected. Because of this gap, there is potentially a small part of the total trace metal pool that was not considered. This gap is not thought to be a substantial portion of the total pool as a comparison between dissolved trace metals filtered at 0.2- and 0.4 μm did not show a significant difference (Fitzsimmons and Boyle, 2012). However, even if a small fraction is missed, the trends and correlations between the operationally defined dissolved and particulate fractions can be used and interpreted. In fact, regardless of used filters, trace metal fractions are all operationally defined and effective cut-offs of used filters vary between brands and change with increasing particle loading. Operational definitions inherently give the possibility of different fractions to be over- or underestimated. For instance, the use of hydroxylamine hydrochloride is known to dissolve some of the higher order Fe-oxides such as hematites (Poulton and Canfield, 2005), potentially leading to an overestimation of the labile fraction. The leachable fraction is arguably a better word for this fraction. However, this method and name are the GEOTRACES community standard and its consistent use allows comparison between data sets.

To understand the cycling of Fe in the ASP region, it is crucial to know where Fe originates from. Sources of Fe to the ASP can be either surface or deep-water sources and will be discussed separately. Surface Fe sources that are known to play a role in the Amundsen Sea are sea ice melt, surface ice-shelf melt, iceberg melt and possibly atmospheric input. Known deep water sources for Fe in the Amundsen Sea are the inflow of CDW and sedimentary inputs (Gerringa et al., 2012; Sherrell et al., 2015). All of these possible sources will be discussed below.

4.1.1. Atmospheric input

In the Southern Ocean, atmospheric input is likely to be negligible as a direct source of DFe (Wagener et al., 2008). For the Amundsen Sea, it has been shown that the atmospheric dust input only contributes <0.1% of the DFe that is required to sustain the phytoplankton blooms (Gerringa et al., 2012; Sherrell et al., 2015). For PFe, the dust flux in the Southern Ocean would yield a steady state concentration of 0.11–31 pM in the upper 10 m of the water column (Planquette et al., 2013). This means that the estimated steady state atmospheric PFe input concentration is at least 35 times lower than total PFe concentrations in the upper 10 m at the open ocean station 53 (Fig. 6). Moreover, the supposed steady state concentration is at least 300 to 1000 times lower than PFe concentrations in the upper 10 m of the ASP and DIS stations. Direct atmospheric dust input to the water column can thus only be responsible for a tiny fraction of total particulate trace metals in the upper water column, especially in the ASP, and is thus not further considered. However, there also might be indirect atmospheric input, for example deposition on sea ice or the ice shelves that reaches the ASP via meltwater. Given that such indirect input is included in the melt water sources, it will not be further investigated here.

4.1.2. Sea ice melt

Sea ice melt (SIM) is a known source of DFe, characterized by DFe that is often largely bound to organic ligands (Lannuzel et al., 2015), though the magnitude of this source can be highly variable (de Jong et al., 2013; Lannuzel et al., 2010). At all stations in the ASP, reduced salinity was observed in the upper meters of the water column, implying melt water influence (Fig. 3). Using $\delta^{18}O$ measurements, we differentiated between sea ice melt and meteoric melt, where the latter includes ice shelf melt (both basal and surface run-off), icebergs and precipitation (Fig. 8). At the inflow- and outflow of CDW at the DIS, as well as at the DIS stations, all collected samples showed positive meteoric melt (MET) fractions and negative SIM fractions. The latter is an indication of sea ice formation on yearly scales (Bauch et al., 2011; Randall-Goodwin et al., 2015; Sherrell et al., 2015; Silvano et al., 2018). In contrast, at the mCDW inflow and shelf break station (st 49 and 52) and open ocean station (st 53), SIM fractions in the surface were positive, indicating net melting of sea ice. Nevertheless, the DFe surface concentrations were low (Fig. 5) at all stations away from the DIS, including those stations with a positive sea ice melt fraction. This could indicate either a very rapid uptake of the released DFe by phytoplankton, or a lack of DFe input associated with sea ice melting. Given that there is no relationship between the SIM fractions and DFe, and that the Chl-a concentrations were relatively low [range 0.58–0.89 $\mu g/m^3$; Table 5) at stations with maximum SIM fractions (Fig. 8A), we postulate that sea ice is not likely the most significant contributor of DFe in this region.

Besides DFe, PFe can be incorporated into sea ice via mechanisms such as sediment resuspension at time of sea ice formation, atmospheric deposition or inclusion of biogenic particles. From experiments on incorporation of iron and organic matter into young Antarctic sea ice, it is known that PFe incorporation in sea ice has a higher enrichment index compared to DFe (Janssens et al., 2016), implying sea ice should be a stronger source of PFe relative to DFe. However, at the stations outside the central polynya (Fig. 2) where we observed positive SIM signatures, PFe concentrations were low (Fig. 5) throughout the entire water column, indicating that SIM was not an important source of PFe in the ASP at the time of sampling either. Despite not appearing as an important source of Fe in our study, SIM has been shown before to play an important role in bloom development by enhancing light penetration (removal of the sea ice but also resulting from enhanced melt-induced stratification in this region) (Schofield et al., 2015; Sherrell et al., 2015). Enhanced stratification due to sea ice melt is indeed observed at stations out of the polynya (Fig. 3B) that coincides with elevated fluorescence (Fig. 3C) indicating that also during our sampling campaign, stratification can play a role in the dynamics of the phytoplankton bloom and likely stimulates the biological assimilation of Fe.

4.1.3. Icebergs and ice-shelf melt as surface source

Icebergs are a known surface source of trace metals to surface waters of the Southern Ocean. (Duprat et al., 2016; Lin et al., 2011; Smith et al., 2007). The large concentration range reported for icebergs makes this source hard to constrain, also because mixing induced by icebergs has been suggested to be an important indirect supply mechanism (Hopwood et al., 2017; Randall-Goodwin et al., 2015; Sherrell et al., 2015). To assess the potential importance of direct iceberg melt input in the ASP, the MET signature (Fig. 8B) could be used. However, this meteoric signature does not allow differentiation between iceberg melt and melt input from the nearby ice shelf as icebergs are most likely derived from this same ice shelf and have a similar $\delta^{18}O$ signature, and thus these two sources are assessed together.

In the surface waters of the central ASP we found no correlation between elevated meteoric melt and DFe or PFe concentrations

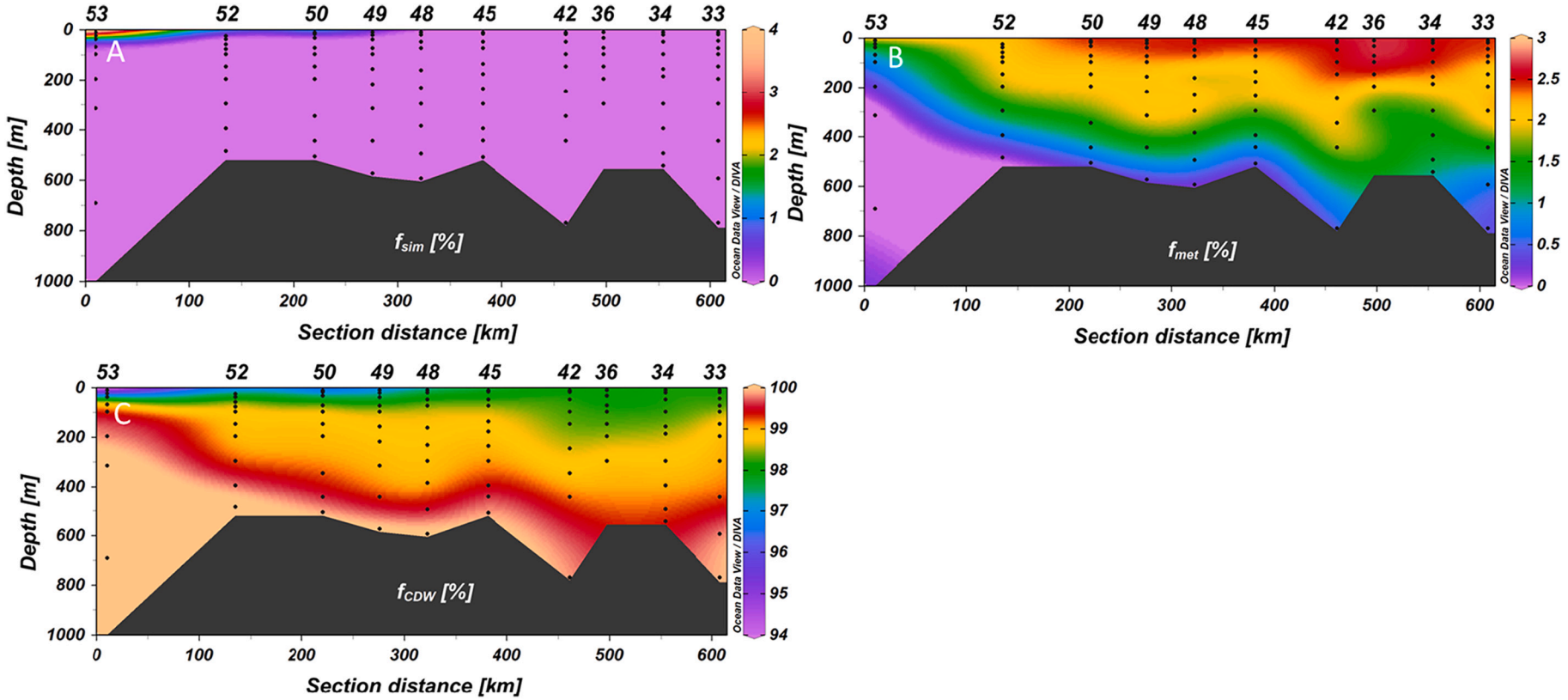

Fig. 8. Transect plots of delta ^{18}O fractions (Tian et al., 2022) of A sea-ice melt B meteoric and C CDW.

(Fig. 7B), implying little influence of iceberg melt and that any ice shelf derived Fe either did not get very far or that there was a decoupling between the $\delta^{18}O$ signal and the transport of Fe. However, the influence of icebergs is likely very localized and could have been missed. Additionally, the indirect iceberg induced vertical mixing could not be assessed with the current data set as no data was obtained in the vicinity of ice bergs. Nevertheless, the absence of clear surface enrichments does imply any such input is either not wide spread, or does not remain in the surface layer long. This is in agreement with an earlier study where near iceberg stations were analyzed, and no increased surface concentrations were reported (Sherrell et al., 2015). With a warming climate, it is possible though, that more icebergs will occur in the ASP and that iceberg melt will have a more prominent role as a source of both DFe and PFe to ASP surface waters, as could the role of DIS melting.

4.1.4. Deep and sedimentary sources

Deep water sources like CDW, sediment sources and basal melt at the DIS have been reported to supply Fe to the ASP (Gerringa et al., 2012; Gerringa et al., 2020; Planquette et al., 2013; Sherrell et al., 2015). The relatively Fe-enriched CDW, with an average DFe of 0.3–0.4 nM (Sedwick et al., 2008; Tagliabue et al., 2012) that flows onto the shelf could be an important source for the ASP phytoplankton bloom after upwelling. At the northernmost station 53, the average DFe (0.38 nM ± 0.06 nM) was in good agreement with earlier observations in the open Southern Ocean (Sedwick et al., 2008; Sieber et al., 2021). Sediment derived input is another source of Fe into CDW while it advects over the shelf. When only mixing between CDW and WW is at play, a linear regression between Fe and salinity is expected, whereby the local CDW and WW endmembers lie on either end of this mixing line. A sedimentary source would lead to Fe concentrations that deviate above the mixing line, whereas scavenging would lead to Fe concentrations below the mixing line. For DFe, most data points within 200 m from the sea-floor were above or on the mixing line, implying indeed a sedimentary source (Fig. 9A) is important, as suggest before for Antarctic shelf seas (Sherrell et al., 2018). On average, this sedimentary source added 0.31 nM ± 0.23 nM DFe to mCDW inflow. Despite these elevated DFe concentrations near the sea-floor, there is little evidence that elevated DFe concentrations in the central ASP close to the sea floor are directly relevant as an Fe source to the euphotic zone where it could affect the ASP phytoplankton productivity. The relatively strong salinity-induced vertical stratification most likely prevented a significant vertical mixing of mCDW and AASW in the central polynya (Fig. 3A) (Randall-Goodwin et al., 2015; Sherrell et al., 2015).

This DFe rich mCDW water, with an average background concentration of 0.38 nM DFe to which the sedimentary source adds on average another 0.31 nM DFe, flows towards the DIS. The relatively high temperature of mCDW leads to melting and the subsequent density change results in upwelling (meltwater pump, St-Laurent et al., 2017). To assess the importance of this ice sheet melting as a potential driver (upwelling) and/or source (actual melt) for the delivery of DFe, the difference between the inflow- and outflow of mCDW was assessed. Local endmembers were used as decribed in section 3.1. We note the following calculation gives a first order assessment of the relative importance of the sources where endmembers were chosen to represent local conditions best. Estimations of concentrations are reported as depth weighted average and a range is given.

For DFe, the weighted average mCDW outflow concentration is lower (0.64 nM, range 0.56–0.69 nM) than the weighted average mCDW inflow concentration (0.75 nM, range 0.49–1.18 nM). It thus appears that basal melt of the DIS does not contribute DFe to the outflow. However, the dilution effect of relatively Fe-poor shelf water mixing with outflowing mCDW and ice shelf meltwater must also be considered. To assess this, a three-endmember mass balance approach was used as described by Tian et al. (2022) The results of this calculation showed that mCDW outflow was composed of 0.44–0.71% ice shelf meltwater, 28–44% shelf water, and 55–72% mCDW inflow. The DFe ice shelf meltwater endmember was estimated to be 4.47 nM [Range: 5.8–12.2 nM]. Thus, there was likely a small contribution of relatively Fe-rich melt water to the outflow. However, given that ice shelf melt was estimated to (on average) only contribute ~0.58% to the overall outflow volume, the resulting average contribution of DFe to the outflow is only on the order of 0.03 nM. Similar results were found in the Ross Sea, where the ice shelf did not noticeably increase DFe concentrations (Gerringa et al., 2015). These results show that during our study, although there likely was DFe input from the DIS, its contribution to the outflow was most likely negligible and hard to distinguish due to the range in observed concentrations in the endmembers as well as the dilution effect from mixing with relatively Fe-poor shelf waters. Overall, the relatively high concentrations in the outflow are principally due to incoming mCDW which was enriched by sedimentary input. Previous studies found a similar DFe concentration in outflow water of 0.7 nM (Sherrell et al., 2015) and 0.4–1.31 nM (Gerringa et al., 2012; Gerringa et al., 2020) compared to 0.64 nM in this study, where the current data suggests that the DFe mainly comes from mCDW and sedimentary input in roughly equal proportions. Such DFe concentrations are elevated relative to ambient shelf water concentrations but still relatively low in comparison to DMn concentrations (see section 3.4).

Besides DFe, PFe plays a role too. The same approach as detailed above for DFe, was used to assess PFe cycling. The calculations showed DFe contributions from melt water at outflow station 36, whereas at outflow station 34, further away from the DIS, the calculations implied lower or even negative contributions. The latter is obviously not physically possible and implies non-conservative behavior of Fe, where scavenging leads to DFe partitioning into the PFe pool and hence lower DFe concentrations than expected based on mixing alone at greater distance from the DIS, and likely also at outflow station 36, on which the below estimates are based.

In contrast to DFe, the average PFe contribution from CDW is negligibly low, but an average addition of 2.50 ± 2.10 nM L-PFe and 9.15 ± 7.30 nM R-PFe from sedimentary sources was estimated (Fig. 9). Unlike for DFe, the average L-PFe outflow concentration (10.79 nM, range: 9.12–13.35 nM) was roughly two times higher than inflow concentrations (4.92 nM, range: 2.15–7.49 nM). For R-PFe, the average outflow concentration (35.64 nM, range: 26.65–40.63 nM) was similarly around two times higher than the inflow concentration (16.11 nM, range: 6.42–24.88 nM). The ice shelf melt endmembers were estimated for both L-PFe and R-PFe at 1478 nM [1148–1712 nM] and 3737 nM [3326–5155 nM] respectively, much higher concentrations than found for DFe, resulting in an estimated contribution from DIS ice shelf melt water of 6.22 nM [5.11–9.85 nM] for L-PFe and 19.74 nM [14.66–27.48 nM] for R-PFe. This is in agreement with an earlier study on total PFe, where near the DIS, PFe concentrations were ranging between 15.43 and 62.00 nM (Planquette et al., 2013). Our results suggest that meltwater from the DIS is a major source of PFe where again the outflow is diluted due to mixing with shelf waters as observed for DFe. Moreover, it seems there is interaction and exchange between DFe and PFe pools as discussed below.

An important factor that controls the solubility and concentrations of Fe in the Southern Ocean is the complexation with iron-binding ligands (Ardiningsih et al., 2020a, 2020b; Boye et al., 2001; Thuróczy et al., 2012). These iron-binding ligands are in competition with scavenging by particulate phases. The observed ligand/DFe ratios in this study were all above 1, with a range of [1.18–11.88] and average of 4.17 ± 2.13. Close to the DIS (st 36 and 42) the ratio was always above 2 indicating that iron-binding ligands were never fully saturated and as such, should be capable of binding more DFe throughout the study region. This was in contrast to the previous study where close to the PIG, ratios were close to 1, indicating that there was only little capacity left to buffer additional DFe at that time and thus there might be temporal and spatial variability (Thuróczy et al., 2012). There was no significant difference in ligand concentrations between stations in this study (Fig. 7A). Only free-iron Fe' showed a trend (Fig. 7B) with lowest concentrations at mCDW

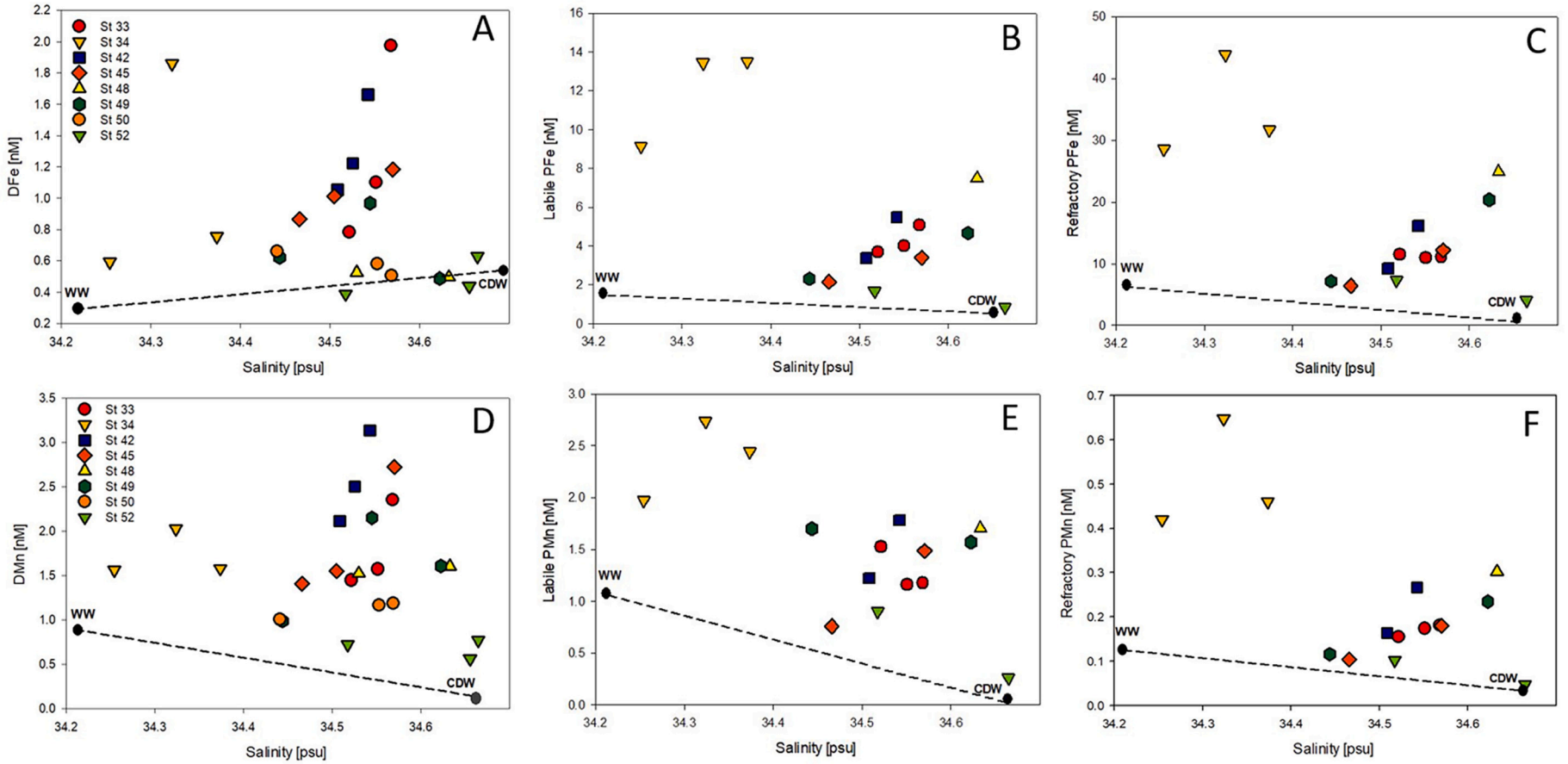

Fig. 9. A DFe vs Salinity with mixing line between WW (st 49, 314 m depth) and CDW (st 53, 788 m depth) and B L-PFe vs Salinity C with mixing line between WW and CDW.

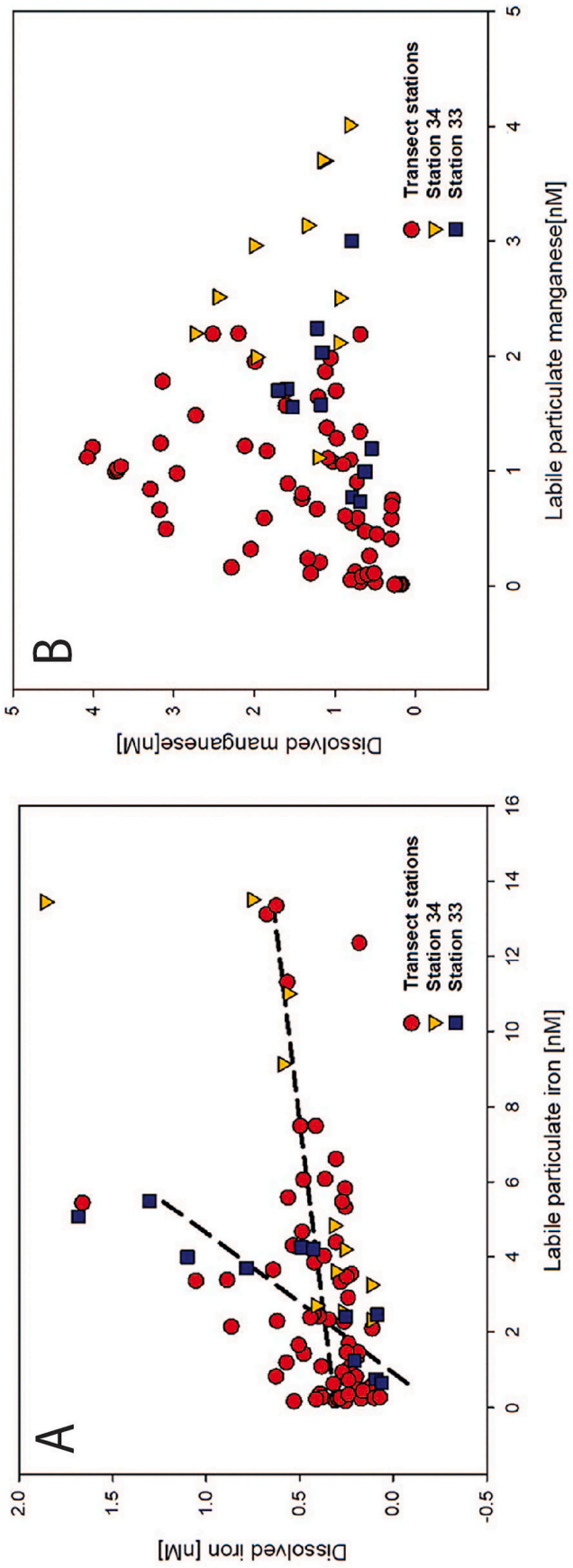

Fig. 10. A Labile PFe vs PFe and B labile PMn vs PMn. Iron has a positive correlation in the outflow stations 34 ($R^2 = 0.622$, $P = 0.004$) and 33 ($R^2 = 0.689$, $P = 0.002$) whereas manganese did not show any significant correlations in the outflow stations.

outflow station 36 and highest concentrations at mCDW inflow station 49. Thus, although Fe-binding ligands were abundant in the study region, they were apparently not strong enough to solubilize PFe and/or maintain elevated DFe concentrations, leading to relatively low Fe' and precipitation of any DFe that might have been released from the DIS. Similar behavior has been observed before in the Arctic Ocean (Ardiningsih et al., 2020a, 2020b; Slagter et al., 2017; Thuróczy et al., 2012) and in the Mediterranean Sea (Gerringa et al., 2017), where reversible scavenging was outcompeting the Fe binding ligands. This can lead to low DFe but does not necessarily result to overall loss of Fe (dissolved and particulate phases) in the water column.

Scavenging of DFe is often considered a loss factor of bioavailable Fe for phytoplankton as particulate phases are susceptible to settling and loss from the euphotic zone. Scavenging results in sink-out of bioavailable Fe in the photic zone and the DFe is thereby lost from phytoplankton. Nevertheless, L-PFe can increase the overall bioavailable (L-PFe + DFe) Fe pool by up to 55% (Milne et al., 2017) and particulate phases can also buffer DFe (via continuous exchange between the fractions) and as such maintain elevated total concentrations as reported for hydrothermal plumes (Fitzsimmons et al., 2017). In such plumes, concentrations of L-PFe are also known to be high, and it has been suggested that in ocean regimes with high particulate Fe loadings, DFe transport may depend on the balance between stabilization in the dissolved phase and the reversibility of exchange onto sinking particles (Fitzsimmons et al., 2017). When DFe is plotted against L-PFe in the CDW outflow, a positive correlation is observed in the CDW outflow stations 34 ($R^2 = 0.62$, $P \leq 0.001$) and 33 (R^2 0.69, $P < 0.001$) (Fig. 10A). This strong positive correlation indicates an (reversible) equilibrium between the two phases through dissolution and re-adsorption, where we postulate that L-PFe possibly buffers and maintains DFe in a certain concentration range, even when there is strong biological consumption of DFe, but this equilibrium between L-PFe and DFe at the same time prevents occurrence of even higher DFe concentrations. Importantly, akin to hydrothermal settings, exchange between the dissolved and particulate phase could enable long range transport of Fe that enters the ASP via the CDW outflow. Alternatively, the observed correlation results from dissolution of Fe from L-pFe where L-pFe is continuously resupplied. However, despite the limited sampling along the outflow in the current study, there are indeed indications for transport away from the DIS rather than continuous supply of new particles. Station 48 (~600 m deep) is located on the eastern flank of the Dotson Trough and thus is situated along the apparent inflow pathway of mCDW. Indeed, the near bottom water was consistent with inflowing mCDW, however, at 200 m depth a decrease in oxygen concentrations and an increase in temperature and macronutrients was observed (Figs. 3 and 4). This implies a meandering outflow or specific outflow branch was located at this location and depth. Besides the macronutrients, PFe, PMn and DMn were also elevated, whereas no clear enrichment in DFe was visible. We suggest this indicates transport of nutrients and metals from the DIS, where the relatively low observed DFe concentrations are most likely the result of the equilibrium between the dissolved and particulate phase that is dominated by the latter phase (Fig. 10A). Specifically, as it is hard to conceive a DMn without any DFe as well from a glacial source (Wehrmann et al., 2014), we postulate DFe was equilibrated rapidly with L-PFe. The contribution of L-PFe to the total pool of Fe (DFe + L-PFe + R-PFe) could be used as an approximation of the potential solubility of PFe sources (Table 6) where it should be noted a small fraction might be missed due to the used filters (see section 4.1). Nevertheless, between the inflow and outflow, there is no significance difference observed in the partitioning between the measured fraction, indicating there is no substantial difference in this potential solubility between sedimentary and ice shelf sources. Additionally, the different distribution patterns of Mn and Fe can provide additional insight into the cycling of Fe in the AP as discussed in the next section.

Table 6
Lithogenic and biogenic contributions of Mn and Fe. Crustal contributions of particulate Mn calculated with crustal ratios of 0.0036 mol Mn/mol. Crustal contributions of particulate Fe calculated with crustal ratios of 0.21 mol Fe/mol Al. Biogenic contributions of particulate Mn and Fe calculated by Southern Ocean diatom metal quotas of 0.28 mmol Mn/mol P and 1.93 mmol Fe/mol P (Twining et al., 2004).

Station	Depth	R-PMn / R-PAl	R-PMn crustal	total Mn/Al	T-PMn crustal	R-PFe / P-RAl	R-PFe crustal	total Fe/ Al	T-PFe crustal	total Mn/ P	biogenic T-PMn	total Fe/P	biogenic T-PFe	L-PMn contribution of T-PMn fraction	L-PFe contribution of T-PFe fraction
	[m]	[mol mol^{-1}]	%	[mol mol^{-1}]	%	[mol mol^{-1}]	%	[mol mol^{-1}]	%	[mmol mol-1]	%	[mmol mol-1]	%	%	%
	769	0.004	85	0.03	13	0.26	81	0.32	65	279	0	3318	0	32	28
	690	0.004	82	0.03	12	0.28	76	0.33	65	386	0	4322	0	39	25
	592	0.004	95	0.04	10	0.28	75	0.32	65	434	0	3901	0	48	23
	443	0.004	89	0.04	10	0.27	78	0.32	65	438	0	3809	0	60	27
	195	0.004	84	0.04	10	0.28	74	0.34	62	425	0	4020	0	57	30
33	146	0.004	89	0.03	12	0.27	79	0.32	67	304	0	3296	0	46	25
	97	0.004	91	0.03	14	0.25	83	0.29	73	46	1	523	0	32	22
	72	0.004	83	0.05	8	0.30	70	0.32	66	3	9	21	9	41	16
	44	0.005	75	0.06	6	0.35	59	0.36	58	3	10	19	10	54	11
	19	0.005	66	0.04	8	0.42	50	0.48	44	3	9	34	6	56	28
	10	0.005	77	0.04	9	0.38	55	0.41	51	3	9	31	6	50	19
	542	0.004	90	0.02	17	0.28	76	0.34	62	564	0	8768	0	54	29
	492	0.004	83	0.02	18	0.29	72	0.34	62	558	0	9432	0	52	22
	393	0.004	87	0.02	17	0.28	75	0.32	65	588	0	9239	0	50	24
	295	0.004	88	0.02	18	0.26	82	0.31	68	438	0	6805	0	48	29
	186	0.003	111	0.02	18	0.26	82	0.30	69	156	0	2311	0	NA	NA
34	156	0.003	106	0.02	17	0.24	86	0.28	75	118	0	1517	0	25	20
	97	0.003	114	0.02	23	0.24	88	0.26	80	12	2	193	1	26	15
	72	0.005	79	0.03	13	0.27	79	0.30	70	6	5	67	3	NA	NA
	48	0.004	95	0.02	15	0.25	86	0.28	76	6	4	72	3	50	18
	20	0.004	101	0.02	16	0.25	85	0.28	74	6	5	75	3	51	19
	9	0.004	101	0.03	14	0.63	33	0.66	32	7	4	188	1	45	12
	295	0.004	91	0.02	22	0.27	79	0.31	68	583	0	11,202	0	45	24
	245	0.004	95	0.02	20	0.26	80	0.32	66	480	0	8319	0	46	28
	196	0.004	93	0.02	20	0.26	81	0.31	68	383	0	6529	0	44	27
36	146	0.003	136	0.01	30	0.22	95	0.25	85	23	1	469	0	21	16
	72	0.003	125	0.01	31	0.23	92	0.26	80	34	1	777	0	19	20
	32	0.003	125	0.01	26	0.24	89	0.27	77	51	1	1015	0	21	20
	9	0.003	127	0.01	29	0.23	93	0.26	81	48	1	983	0	20	20
	769	0.004	91	0.03	13	0.24	88	0.28	74	674	0	7091	0	34	24
	690	0.004	81	0.03	11	0.25	84	0.30	70	414	0	3744	0	34	25
	641	0.004	89	0.03	12	0.25	84	0.30	71	547	0	5585	0	57	25
	542	0.005	77	0.03	12	0.27	79	0.31	67	634	0	6462	0	61	26
	344	0.004	101	0.04	10	0.24	88	0.29	73	331	0	2717	0	52	26
42	245	0.003	131	0.02	19	0.19	112	0.22	95	161	0	1843	0	21	19
	97	0.003	126	0.01	30	0.20	104	0.24	88	45	1	893	0	11	23
	72	0.003	131	0.01	33	0.20	104	0.24	88	52	1	1144	0	NA	NA
	47	0.003	122	0.01	31	0.22	97	0.24	86	24	1	507	0	20	17
	18	0.003	125	0.01	33	0.22	95	0.25	84	13	2	295	1	14	18
	11	0.003	120	0.01	32	0.23	91	0.25	84	14	2	306	1	19	14
	507	0.004	91	0.03	11	0.27	78	0.31	69	493	0	4606	0	35	20
	442	0.005	78	0.03	11	0.29	74	0.33	63	364	0	3621	0	33	23
	394	0.004	85	0.03	11	0.29	73	0.33	64	551	0	5798	0	52	23
	345	0.003	106	0.03	11	0.32	67	0.36	59	475	0	5355	0	14	19
45	235	0.004	96	0.03	10	0.26	82	0.30	70	316	0	2751	0	54	22
	176	0.004	92	0.04	10	0.27	78	0.31	67	256	0	2217	0	48	21
	97	0.004	100	0.03	12	0.25	86	0.29	72	50	1	501	0	NA	NA
	73	0.004	84	0.03	13	0.26	82	0.28	74	7	4	71	3	13	19
	47	0.005	77	0.04	10	0.34	62	0.38	55	3	9	31	6	34	24

(*continued on next page*)

Table 6 (*continued*)

Station	Depth	R-PMn / R-PAl	R-PMn crustal	total Mn/Al	T-PMn crustal	R-PFe / P-RAl	R-PFe crustal	total Fe/ Al	T-PFe crustal	total Mn/ P	biogenic T-PMn	total Fe/P	biogenic T-PFe	L-PMn contribution of T-PMn fraction	L-PFe contribution of T-PFe fraction
	[m]	[mol mol^{-1}]	%	[mol mol^{-1}]	%	[mol mol^{-1}]	%	[mol mol^{-1}]	%	[mmol mol-1]	%	[mmol mol-1]	%	%	%
	15	0.004	89	0.05	8	0.34	61	0.40	52	2	11	21	9	37	25
	10	0.004	92	0.03	12	0.31	69	0.35	60	3	9	35	6	61	19
48	592	0.003	111	0.02	19	0.27	79	0.31	69	455	0	7355	0	44	23
	444	0.003	111	0.03	14	0.25	83	0.31	69	470	0	5647	0	69	25
	231	0.004	93	0.03	11	0.26	82	0.31	69	454	0	4226	0	53	25
	96	0.003	110	0.02	17	0.24	88	0.28	76	124	0	1581	0	36	22
	47	0.003	109	0.02	18	0.25	84	0.28	74	12	2	174	1	27	19
	10	0.005	71	0.04	9	0.45	46	0.45	47	3	11	30	6	67	12
49	572	0.003	124	0.02	18	0.25	84	0.28	75	378	0	5233	0	46	18
	494	0.004	81	0.06	6	0.28	76	0.32	65	305	0	1587	0	60	23
	443	0.004	81	0.04	8	0.27	77	0.31	67	350	0	2568	0	61	22
	314	0.004	84	0.04	9	0.27	79	0.27	79	273	0	1827	0	51	18
	216	0.003	113	0.03	13	0.23	90	0.27	78	138	0	1294	0	47	20
	156	0.004	100	0.03	11	0.24	88	0.28	76	98	0	813	0	35	18
	97	0.004	96	0.03	14	0.25	84	0.22	96	46	1	381	1	22	16
	69	0.004	90	0.03	12	0.26	79	0.28	74	13	2	128	2	6	12
	38	0.003	108	0.03	12	0.21	101	0.26	81	2	12	21	9	42	24
	21	0.005	68	0.04	9	0.53	39	0.43	49	2	14	22	9	45	18
	10	0.005	76	0.04	9	0.37	57	0.39	54	2	14	18	11	54	17
52	483	0.004	98	0.02	17	0.32	66	0.34	62	150	0	2407	0	21	13
	394	0.005	79	0.04	9	0.33	64	0.36	59	315	0	2824	0	52	17
	295	0.007	52	0.09	4	0.35	60	0.40	53	171	0	807	0	44	19
	146	0.005	73	0.10	3	0.34	62	0.39	54	79	0	296	1	45	18
	97	0.004	82	0.06	6	0.33	65	0.39	55	20	1	125	2	15	22
	57	0.005	80	0.05	7	0.33	63	0.40	52	9	3	67	3	8	19
	25	0.006	61	0.07	5	0.43	49	0.47	45	2	14	13	15	14	27
	9	0.007	53	0.11	3	0.44	48	0.48	43	2	16	8	24	35	18
53	1015	0.004	87	0.02	19	0.41	52	0.51	41	13	2	345	1	9	16
	789	0.003	108	0.02	23	0.34	61	0.49	43	7	4	222	1	7	23
	690	0.004	99	0.02	21	0.36	58	0.50	42	7	4	206	1	5	11
	542	0.002	153	0.01	34	0.24	87	0.34	62	8	3	257	1	6	16
	394	0.003	109	0.01	27	0.35	60	0.46	46	6	4	221	1	4	21
	196	0.003	128	0.02	20	0.30	71	0.37	56	9	3	184	1	6	23
	97	0.004	86	0.02	16	0.48	43	0.56	38	4	7	108	2	4	28
	67	0.004	97	0.01	25	0.41	52	0.47	45	2	13	71	3	6	30
	37	0.004	84	0.04	10	0.40	52	0.51	41	1	22	19	10	10	30
	24	0.005	74	0.06	6	0.63	33	0.59	36	1	22	13	14	14	21
	10	0.006	58	0.06	6	0.42	50	0.48	43	2	18	14	14	12	24

Crustal contributions of particulate Mn calculated with crustal ratios of 0.0036 mol Mn/mol. Crustal contributions of particulate Fe calculated with crustal ratios of 0.21 mol Fe/mol Al. Biogenic contributions of particulate Mn and Fe calculated by Southern Ocean diatom metal quotas of 0.28 mmol Mn/mol P and 1.93 mmol Fe/mol P (Twining et al., 2004).

4.2. Sources of dissolved and particulate Mn as tracer of Fe

The potential sources of Mn are similar to those of Fe. Atmospheric deposition is a potential source of DMn and is important in other parts of the world's ocean (Baker et al., 2006). However, the crustal abundance of Mn is much lower than for Fe (Hu and Gao, 2008) and since atmospheric deposition was not a significant source of Fe to the ASP, we also assume that there is very limited atmospheric deposition of Mn to the region. There is not much known about Mn in icebergs and their potential role as a source in the Southern Ocean. However, from size fractionation studies in fast ice, it is known that 57% of Mn is present in the form of larger particles whereas for Fe this is close to 97% (Lannuzel et al., 2014). Assuming the partitioning between the dissolved and particulate phase is similar in glacial ice, this could be an indication that when icebergs melt, the ratio of released DMn/PMn is higher than DFe/PFe. Similar to Fe, however, based on low surface DMn concentrations we did not see any indication that melting icebergs play a major role for Mn cycling in the ASP.

Oxidation of Fe is thought to be much faster than Mn, and such oxidation may yield an amorphous colloidal Fe oxyhydroxide phase (Landing and Bruland, 1987). Near-shore removal processes are more intense for DFe than for DMn and as such, DMn in the surface mixed layer can remain elevated much further offshore than DFe (Landing and Bruland, 1987). Therefore, DMn could potentially be used as a tracer for DFe. In CDW, the average DMn concentration was relatively low (0.20 ± 0.03 nM), but slightly higher than earlier observations (0.11 nM; Sherrell et al., 2015) and lower than reported values for mCDW (0.34–0.58 nM; Hatta et al., 2017). The higher concentrations in CDW at station 53 compared to previous observations in the region as well as our observations further off shore (data not shown), indicates that CDW already carries some shelf derived Mn input at this near shelf location. Sediments have been suggested as a major source of Mn to the Southern Ocean (Bucciarelli et al., 2001; Latour et al., 2021; Middag et al., 2011; Sherrell et al., 2015). Indeed, the mixing line approach between WW and mCDW showed that for DMn, all samples fall above this line, indicative of a sedimentary DMn source addition (Fig. 9). The average DMn input from the sediment was estimated to be 0.87 nM ± 0.58 nM, showing that the sediment-derived input is relatively more important for DMn than for DFe. For DMn, the weighted average mCDW outflow concentration is higher (average 2.00 nM, range 1.55–2.51 nM) than the weighted average inflow concentration (average 1.61 nM, range 1.41–2.73 nM), indicating a much higher DMn contribution from meltwater of the DIS than was seen for DFe. Indeed, the estimated DMn ice shelf melt water endmember was 44.13 nM [−31.7–152.1 nM], which leads to an estimated contribution of 0.27 nM DMn to the outflow in contrast to the negligible DFe contribution from DIS melt. Similar to DFe, DMn highest ice shelf melt contributions were observed at the ice shelf outflow station (st 36) whereas inferred negative contributions at mCDW outflow station 34 imply non-conservative behavior for Mn as well. Nevertheless, overall DMn concentrations were higher than DFe near the DIS implying DFe was even more prone to non-conservative behavior than DMn. This is also visible in the partitioning between DMn and PMn where the contribution of the particulate phase to the overall pool is lower for Mn than for Fe (Figs. 5 and 6). Similar to Fe, the contribution of L-PMn to the total pool of Mn (DMn + L-PMn + R-PMn) did not show a signific difference between the inflow and outflow, indicating there is no substantial difference in this potential solubility between sedimentary and ice shelf sources. There are however trends observed in the in partitioning between the upper 100 m surface layer and the deeper waters along the transect. Where L-PFe remains similar (20 ± 5% vs 22 ± 4%), L-PMn has a lower labile fraction in surface waters (29% ± 18 vs 40% ± 18). Although these values show large variation, it gives an indication that in the surface L-PFe is a more important source for phytoplankton compared to L-PMn or sedimentary sources are more for L-PMn than it is for L-PFe.

For PMn, mCDW was found to be a negligible source, and sedimentary input was estimated to contribute 1.03 nM ± 0.51 nM L-PMn and 0.19 nM ± 0.15 nM R-PMn (Fig. 9). Additionally, the average L-PMn outflow concentration (average 2.08 nM, range 1.98–2.20 nM) was around two times higher than the inflow concentration (average 1.29 nM, range 0.75–1.70 nM) and the ice shelf melt endmember was estimated at 191 nM [163–212 nM] which translates to a 1.00 nM [0.85–1.16 nM] contribution in the outflow. The average R-PMn outflow concentration (0.52 nM, range 0.42–0.60 nM) was around 2.5 times higher than the inflow concentration (0.21 nM, range 0.10–0.30 nM) where the ice shelf melt endmember concentration (60 nM, range 45.2–80.2 nM) results in a 0.31 nM (range 0.25–0.43 nM) contribution of R-PMn in the outflow.

These estimations suggest that meltwater from the DIS contributed PMn to the ASP during our study, but far less than was seen for PFe, in contrast to the dissolved phase. While estimated L-PMn ice shelf concentrations were only slightly lower than DMn, the R-PMn ice shelf contribution was more than four times lower. Additionally, at the DIS, DMn input resulted in elevated surface concentrations which were not seen for DFe. These findings are similar to a study done along the West Antarctic Peninsula shelf, where local glacial meltwater appears to be an important DMn source, but is not a large direct input of DFe to this biological hotspot (Seyitmuhammedov et al., 2021; Sherrell et al., 2018). Unlike for Fe, there was no positive correlation found between L-PMn and DMn (Fig. 10B) in the outflow implying no or at least less exchange between these phases than suggested for Fe. St-Laurent et al. (2019) suggested, based on recent modelling efforts, that the micronutrient Fe exhibits strong seasonality, where scavenging by biogenic particles and remineralization play large compensating roles. This also implies there is continuous exchange between the DFe and L-PFe pools. However, these modelling efforts (St-Laurent et al., 2017) only take DFe and biogenic PFe into account and thereby may miss the crucial role of dissolved organic ligands and non-biogenic PFe in the distribution of DFe in the ASP.

4.3. Origin of particulate Fe and Mn

4.3.1. Lithogenic contribution

As described above, the particulate phases are important in the cycling of both metals, but most notably Fe. To better understand the role of the particulate fraction, we estimate the origin of the particles from various sources, specifically the potential lithogenic, sedimentary and biogenic contribution to the total PFe and PMn concentration. Please note these are potential contributions based on operational definitions or assumptions about elemental ratios as detailed below.

Lithogenic particles are assemblages of crustal derived minerals that transit the water column largely unaltered (Ohnemus and Lam, 2015) and to estimate the potential lithogenic contribution, PFe/PAl and Mn/PAl ratios in mean crustal material can be used (Planquette et al., 2013). The element Al occurs in relatively high abundance in the earth's crust and has no key biological functions (De Baar et al., 2017). All particulate Al (PAl) is therefore assumed to be of crustal origin and a linear regression of PFe or PMn against PAl can be used to evaluate if there is a consistent potential lithogenic contribution to the particulate trace metal pool. The study area is close to a source of crustal material (glacial debris) and it thus likely that a substantial part of Fe is in the same mineral forms as the crustal material. A strong positive correlation was found between R-PFe and R-PAl (R^2 0.93, $p < 0.05$) over the entire water column (Fig. 11A), indicating that R-PFe has a consistent lithogenic source in both the euphotic zone and deeper waters. The R-PFe pool consists on average of 75% ± 16% lithogenic particles, ranging from 33% (station 34, 9 m depth) to 100% (st 42, 72–245 m; station 49, 38 m) based on an upper crustal PFe/PAl ratio of 0.21 mol mol^{-1} (Taylor and McLennan, 1985, 1995). The total PFe (T-PFe = R-PFe + L-PFe) lithogenic contribution is on average 65% ± 14% (Table 6), which overlaps with the average for the R-PFe pool, but is somewhat lower, indicating a contribution of another source to the smaller L-PFe pool.

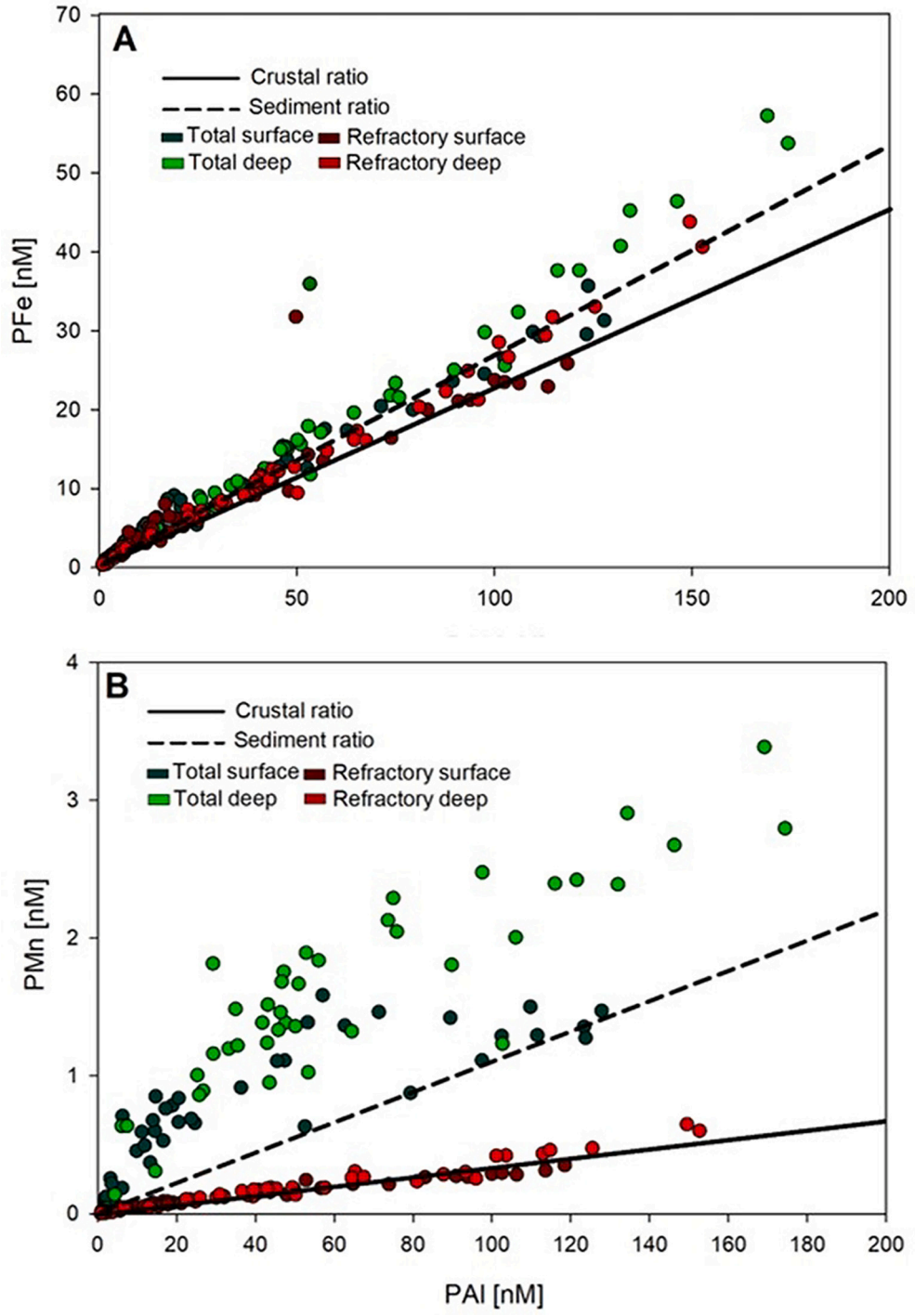

Fig. 11. A Refractory and total PAl and PFe and B Refractory and total PAl and PMn.

Besides the direct input of unaltered crustal material, also resuspended surface sediments are a possible source of PFe. Here it is assumed that an unsorted resuspension source has a total PFe/PAl ratio of 0.26 mol mol^{-1}, and that samples with a higher ratio have an additional unknown Fe source (Angino, 1966; Planquette et al., 2013). For R-PFe, the majority of the samples fell between the crustal and sediment ratio (Fig. 11A). However, when total T-PFe is assessed, most samples fall on or above the sediment ratio. Previously, it was suggested that T-PFe throughout the Amundsen Sea is dominated by inputs of a mixture of unweathered crustal particles and sedimentary authigenic Fe (Planquette et al., 2013). Our data suggest that R-PFe was a mixture of sedimentary and crustal particles, whereas the T-PFe pool also contained particles that were above the two mixing lines. These mainly labile particles are most likely authigenic Fe phases as discussed in section 4.3.3.

For PMn, the PMn/PAl crustal ratio of 0.0034 mol mol^{-1} was used to estimate the lithogenic contribution (Taylor and McLennan, 1985). We find that R-PMn is dominated almost entirely by crustal particles with an average of 89% ± 11% (Table 6). Some of the estimated contributions exceeded 100%, which were mostly samples close to the seafloor. This implies there is a non-crustal source of PMn as well. Nevertheless, for total PMn (T-PMn) the estimated average lithogenic contribution is only 15% ± 8% (Table 6), implying the non-crustal contribution was mainly present in the (larger) labile fraction. The T-PMn concentration is much lower than for T-PFe and the estimated T-PMn lithogenic contribution is

in good agreement with earlier reported values (Planquette et al., 2013). Similar to T-PFe, the T-PMn samples all fall on or above the sediment line (Fig. 11B) implying that like for Fe, there must indeed be another labile contribution to the particulate Mn pool as well. Planquette et al. (2013) reported that especially small PMn particles belong to this unknown endmember, where the current data clearly indicates such particles occur in the labile fraction and thus are likely biogenic or authigenic whereas the R-PMn is mainly of lithogenic origin.

4.3.2. Biogenic contribution

Biogenic particulate trace metals are defined as trace metals that are incorporated in biotic particles (Collier and Edmond, 1984) and are mostly expected in the labile fraction. Particulate phosphate (PP) is assumed to be fully biogenic. However, up to 25% of the total PP was measured in the refractory phase. This could be related to the high particle loading on the filters and the operational definition of the standardised leaching procedure used. Alternatively, a relatively refractory biogenic molecules might have been present. Therefore, the total PP concentration is used here to calculate a linear regression between PP and the particulate trace metal fractions, which is thus indicative of a consistent biogenic component to the particulate trace metal pool (Planquette et al., 2013). This variable biogenic component can be estimated (Table 6). By multiplying measured particulate phosphorus with previously reported Southern Ocean diatom Fe/P and Mn/P ratios from individual cells (respectively 1.93 and 0.28 mmol mol^{-1}) (Twining et al., 2004), we estimated biogenic metal concentrations which can be expressed as contributions relative to the total concentrations. Biogenic T-PFe had still negligible contributions throughout the water column ($\leq$ 1%) at the ice shelf stations (st 36 and 42) and below 100 m at the remaining stations, but in the upper 100 m of the central ASP, the T-Pfe contribution was up to 24%. The estimated biogenic T-PMn distribution was on average $\leq$ 2% below 100 m, but contributions went up to 22% in the upper 100 m.

It is somewhat surprising that the calculated biogenic contributions for both T-PFe and T-PMn are relatively low in the surface layer, considering that sampling took place during the spring-summer bloom and high Chl-a standing stock was encountered. However, we may be underestimating biogenic T-PFe and T-PMn with the used approach. For example, there could have been a preferential remineralization of P relative to Fe and Mn, resulting in higher phytoplankton and detritus Fe/P and Mn/P ratios compared to the diatom ratio used for the calculation (King et al., 2012). Furthermore, detritus is usually enriched with bacterial biomass, which may also have higher Fe/P ratios (Tortell et al., 1996). Another possibility is that there was a different metal-P ratio at the ASP bloom at the time of our sampling. Prelimanary data (unpublished results) from a bioassay experiment, which started near the coast and was supplemented with additional Fe, during our expedition (limited lithogenic influence over the course of the experiment) indicates that the particulate Fe/P and Mn/P ratios were higher than the single cell diatom ratios reported by Twining et al. (2004). Using such higher ratios inherently leads to a higher estimated biogenic contribution with stations on the northern side of the transect (st 45, 49, 50, 52 and 53) starting to exceed 100% in the surface waters. Such high contributions were mostly located on the outside the ASP, which could imply that the high Fe and Mn ratio that is used for this calculation is valid near the coast and near trace metal sources, but that this ratio decreases towards the open ocean where communities are more Fe limited. It is well established that phytoplankton may adjust their Fe-uptake depending on conditions (Strzepek et al., 2019), potentially even in a relatively small study region as the current data suggests. Other studies also showed that in areas where there is direct dust input or sediment resuspension in shallow regions, Fe uptake is significantly higher than in areas with lower Fe input, indicating an opportunistic uptake approach (luxury Fe uptake) from phytoplankton species (e.g. Boyd et al., 2012; Buitenhuis and Geider, 2010; Sunda and Huntsman, 1995; Twining et al., 2021). Overall, the current results confirm that estimating contributions with a fixed ratio is probably inaccurate, even for a relatively small study region. The true ratio is likely dynamic depending on supply and species composition, where the use of our current bioassay ratios suggests a decreasing uptake ratio with increasing distance from the coast.

4.3.3. Authigenic contribution

Above (section 4.3.1.) it was discussed that our data indicates a third endmember (other than lithogenic or sediments), notably in the labile fraction that could be biogenic or authigenic. Given that, especially in the deep, the biogenic contribution and the T-PP was indeed limited (see above section 4.3.2.), L-PFe and L-PMn in the deeper water column must have existed for a large part of a third endmember, which was most likely composed of authigenic particles. These particles likely result from redox cycling during early diagenesis or authigenic PFe and PMn formation in the water column (Planquette et al., 2013). Authigenic particles are abiotically derived and produced and cycled in situ, for example Fe and Mn oxyhydroxides (Ohnemus and Lam, 2015). To investigate the potential composition of these authigenic particles, the excess of L-PFe and L-PMn can be assessed by calculating how much more L-PFe and L-PMn is there in excess of the sediment ratio line (Fig. 11A, B). This approach ignores any lithogenic contributions (i.e. assumes all labile is authigenic) and resulted in an average excess L-PFe/L-PMn ratio of 4.04 but there was no significant correlation found between the excess metal concentrations (R^2 0.29, $p > 0.05$) implying variable and/or multiple endmembers exists. However, when only the outflow stations 36 and 34 are assessed at full depth, a correlation was found between the estimated excess concentrations of L-PFe and L-PMn (R^2 0.87, $p < 0.05$; not shown). This strong correlation points to a consistent labile (authigenic) source close to the DIS but further away apparently other sources become important as well. The ratio close to the DIS for this inferred authigenic source is very rich in Fe relative to Mn (L-PFe/L-PMn ratio of 5.73) consistent with our hypothesis more DFe than DMn precipitates in the DIS outflow (see section 4.1.4) but the overall composition and structure of these particles remains unknown and should be further investigated in future studies.

5. Conclusions

In the ASP, phytoplankton blooms can only be sustained with a constant input of trace metals. The dissolved trace metal fraction has been studied widely, since this is considered to be the most bioavailable fraction. However, this study shows that based on DFe alone, it appeared that the DIS does not contribute a significant amount of DFe to the ASP (Fig. 12), in contrast to CDW and benthic sediments, which seem to be the biggest sources of DFe in the ASP. Previous studies already

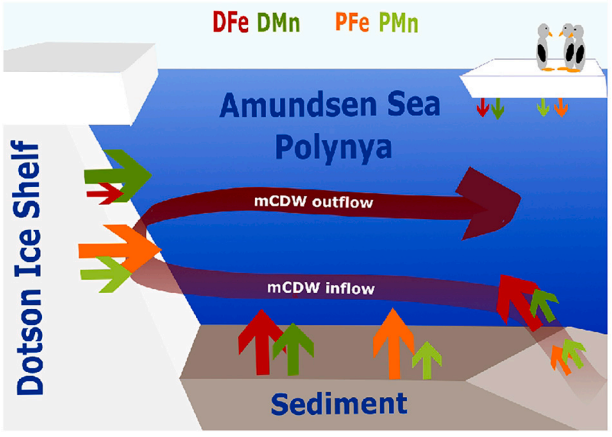

Fig. 12. Conceptual figure of the Fe and Mn sources in the Amundsen Sea Polynya.

acknowledged the importance of the DIS outflow (Gerringa et al., 2012; Planquette et al., 2013; Sherrell et al., 2015) where in this study we were able to deconvolve the contributions of the various contributing sources and underline the importance of the particulate fraction. From the distribution of Mn we learn that there that there are dissolved trace metals being released from the DIS, as found in previous studies. We propose it is thus highly likely that DFe is also released from the DIS but this DFe quickly equilibrates with the labile particulate pool where exchange buffers the DFe pool.

When PFe and the interaction between DFe and PFe are considered, we demonstrate that the DIS is indeed an important source of Fe into the ASP. Iron-binding ligand data suggests that ligands were available, but were most likely not strong enough to compete for DFe against scavenging particles and maintain Fe in solution in a concentration close to that of the ligands. We suggest that the meltwater pump brings relatively high DFe and DMn from mCDW into the surface ocean and is thus a driving mechanism rather than the ice sheet being a source as such. In contrast, ice sheet melt is the major source of PFe and PMn to the ASP and likely an indirect source of dissolved metals (Fig. 12).

This study gives new insights in the interaction between dissolved and particulate fractions of Fe and Mn. Most of the refractory particulate Fe and Mn appear from a lithogenic source, whereas the labile particulate fraction in deep waters (>100 m depth) likely consists of authigenic particles. In the surface layer, more particles of a biogenic origin were observed for both T-PFe and T-PMn. However, there is a huge range in calculated biogenic contributions depending on the used metal to P ratio and thus the chosen ratio, either from a previously reported diatom ratio or a ratio retrieved from an in-situ bioassay experiment, has a strong effect on the contribution calculation and interpretations. This underlines that uptake ratio estimates do not necessarily capture natural variability and we propose to look at different approaches to give a range for any biogenic contribution calculations.

In the future, climate change may cause a higher heat flux of mCDW towards the DIS, thus promoting more melting of the DIS. This will most likely cause an increased input of PFe and PMn into the ASP and the current data suggests that this might lead to additional DFe supply due to the buffering of the DFe pool by L-PFe. Phytoplankton blooms could be potentially longer sustained in the summer season before either iron or manganese becomes limiting. From previous incubation experiments done under sufficient light conditions it is known that all available nitrate was drawdown in both control as well as Fe addition treatment groups (Alderkamp et al., 2015). Nevertheless, even when Fe is not limiting, a higher influx of Fe could lead to increased photosynthesis rates in the central ASP, and can potentially increase the water column productivity by 1.7-fold (Alderkamp et al., 2015), illustrating that enhanced supply of Fe (and potentially Mn) can lead to faster consumption of macronutrients. This could result in a shorter bloom or productive period, affecting the local ecosystem and perhaps result in higher export efficiency, but this remains speculative as additional mCDW would also supply more macronutrients.

Funding

This work is supported by the Dutch Research Council (NWO) (grant number ALWOO.2016.020); The Utrecht University-NIOZ collaboration and the Korea Polar Research Institute (KOPRI) (grant number PE21110). We want to acknowledge NSF for awarding Tim Conway (OCE2123354).

Declaration of Competing Interest

None.

Acknowledgements

We would like to thank the Korea Polar Research institute (KOPRI) for giving us access to this remote region with their R/V Araon. We would like to thank the captain and the crew of the R/V Araon, as well as all the scientists onboard, for their assistance and support during the expedition ANA08B. This study was approved as a GEOTRACES process study (GPpr12). The Figs. 3–6 and 8 were made using ODV version 5.3.0 (Schlitzer, 2021). We also would like to thank Dr. Willem van de Poll from the Faculty of Science and Engineering, University of Groningen, the Netherlands, for the assistance with the analysis of the Chl-a concentration as well as Sven Ober and all the colleagues from NIOZ National Marine Facilities (NMF) for the preparation of Titan CTD and other equipment. We are grateful to Patrick Laan (NIOZ) for all the help with the ICP-MS analyses. Piet ter Schure and his team from DMT Marine Equipment are acknowledged for their great help with the winch setup for the Titan sampling system used on R/V Araon, as without their amazingly fast response to assemble a winch last minute, this research would not have been possible.

Appendix A. Supplementary data

Supplementary data to this article can be found online at https://doi.org/10.1016/j.marchem.2022.104161.

References

Abualhaija, M.M., van den Berg, C.M., 2014. Chemical speciation of iron in seawater using catalytic cathodic stripping voltammetry with ligand competition against salicylaldoxime. Mar. Chem. 164, 60–74.

Alderkamp, A.-C., Mills, M.M., van Dijken, G.L., Arrigo, K.R., 2013. Photoacclimation and non-photochemical quenching under in situ irradiance in natural phytoplankton assemblages from the Amundsen Sea, Antarctica. Mar. Ecol. Prog. Ser. 475, 15–34.

Alderkamp, A.-C., Van Dijken, G.L., Lowry, K.E., Connelly, T.L., Lagerström, M., Sherrell, R.M., Haskins, C., Rogalsky, E., Schofield, O., Stammerjohn, S.E., 2015. Fe availability drives phytoplankton photosynthesis rates during spring bloom in the Amundsen Sea Polynya, AntarcticaFe availability drives photosynthesis in Amundsen Sea Polynya. Elementa 3.

Angino, E.E., 1966. Geochemistry of Antarctic pelagic sediments. Geochim. Cosmochim. Acta 30 (9), 939–961.

Ardiningsih, I., Krisch, S., Lodeiro, P., Reichart, G.-J., Achterberg, E.P., Gledhill, M., Middag, R., Gerringa, L.J., 2020a. Natural Fe-binding organic ligands in Fram Strait and over the Northeast Greenland shelf. Mar. Chem. 224, 103815.

Ardiningsih, I., Seyitmuhammedov, K., Sander, S.G., Stirling, C.H., Reichart, G.-J., Arrigo, K.R., Gerringa, L.J., Middag, R., 2020b. Sources of Fe-binding organic ligands in surface waters of the western Antarctic peninsula. Biogeosci. Discuss. 1–25.

Arrigo, K.R., Van Dijken, G.L., 2003. Phytoplankton dynamics within 37 Antarctic coastal polynya systems. J. Geophys. Res. Oceans 108 (C8).

Arrigo, K.R., van Dijken, G.L., 2015. Continued increases in Arctic Ocean primary production. Prog. Oceanogr. 136, 60–70.

Baker, A.R., Jickells, T.D., Witt, M., Linge, K.L., 2006. Trends in the solubility of iron, aluminium, manganese and phosphorus in aerosol collected over the Atlantic Ocean. Mar. Chem. 98 (1), 43–58. https://doi.org/10.1016/j.marchem.2005.06.004.

Bauch, D., Hölemann, J., Andersen, N., Dobrotina, E., Nikulina, A., Kassens, H., 2011. The Arctic shelf regions as a source of freshwater and brine-enriched waters as revealed from stable oxygen isotopes. Polarforschung 80 (3), 127–140.

Berger, C.J., Lippiatt, S.M., Lawrence, M.G., Bruland, K.W., 2008. Application of a chemical leach technique for estimating labile particulate aluminum, iron, and manganese in the Columbia River plume and coastal waters off Oregon and Washington. J. Geophys. Res. Oceans 113 (C2).

Biller, D.V., Bruland, K.W., 2012. Analysis of Mn, Fe, Co, Ni, Cu, Zn, Cd, and Pb in seawater using the Nobias-chelate PA1 resin and magnetic sector inductively coupled plasma mass spectrometry (ICP-MS). Mar. Chem. 130, 12–20.

Boyd, P.W., Arrigo, K.R., Strzepek, R., van Dijken, G.L., 2012. Mapping phytoplankton iron utilization: insights into Southern Ocean supply mechanisms. J. Geophys. Res. Oceans 117 (C6). https://doi.org/10.1029/2011JC007726.

Boyd, P.W., Ellwood, M.J., Tagliabue, A., Twining, B.S., 2017. Biotic and abiotic retention, recycling and remineralization of metals in the ocean. Nat. Geosci. 10 (3), 167–173. https://doi.org/10.1038/ngeo2876.

Boye, M., van den Berg, C.M., de Jong, J.T., Leach, H., Croot, P., De Baar, H.J., 2001. Organic complexation of iron in the Southern Ocean. Deep-Sea Res. I Oceanogr. Res. Pap. 48 (6), 1477–1497.

Brand, L.E., Sunda, W.G., Guillard, R.R., 1983. Limitation of marine phytoplankton reproductive rates by zinc, manganese, and iron 1. Limnol. Oceanogr. 28 (6), 1182–1198.

Browning, T.J., Achterberg, E.P., Engel, A., Mawji, E., 2021. Manganese co-limitation of phytoplankton growth and major nutrient drawdown in the Southern Ocean. Nat. Commun. 12 (1), 1–9.

Bucciarelli, E., Blain, S., Tréguer, P., 2001. Iron and manganese in the wake of the Kerguelen Islands (Southern Ocean). Mar. Chem. 73 (1), 21–36. https://doi.org/10.1016/S0304-4203(00)00070-0.

Buitenhuis, E.T., Geider, R.J., 2010. A model of phytoplankton acclimation to iron–light colimitation. Limnol. Oceanogr. 55 (2), 714–724.
Chester, R., Hughes, M.J., 1967. A chemical technique for the separation of ferro-manganese minerals, carbonate minerals and adsorbed trace elements from pelagic sediments. Chem. Geol. 2, 249–262. https://doi.org/10.1016/0009-2541(67)90025-3.
Collier, R., Edmond, J., 1984. The trace element geochemistry of marine biogenic particulate matter. Prog. Oceanogr. 13 (2), 113–199. https://doi.org/10.1016/0079-6611(84)90008-9.
Cullen, J.T., Sherrell, R.M., 1999. Techniques for determination of trace metals in small samples of size-fractionated particulate matter: phytoplankton metals off Central California. Mar. Chem. 67 (3–4), 233–247.
Cutter, G., et al., 2017. Sampling and Sample-Handling Protocols for GEOTRACES Cruises, Version 3.0. GEOTRACES Cookbook.
De Baar, H.J.W., Timmermans, K.R., Laan, P., De Porto, H.H., Ober, S., Blom, J.J., Bakker, M.C., Schilling, J., Sarthou, G., Smit, M.G., Klunder, M., 2008. Titan: a new facility for ultraclean sampling of trace elements and isotopes in the deep oceans in the international Geotraces program. Mar. Chem. 111 (1), 4–21. https://doi.org/10.1016/j.marchem.2007.07.009.
De Baar, H.J.W., van Heuven, S., Middag, R., 2017. Ocean biochemical cycling and trace elements. In: Encyclopedia of Earth Sciences Series.
de Jong, J., Schoemann, V., Maricq, N., Mattielli, N., Langhorne, P., Haskell, T., Tison, J.-L., 2013. Iron in land-fast sea ice of McMurdo Sound derived from sediment resuspension and wind-blown dust attributes to primary productivity in the Ross Sea, Antarctica. Mar. Chem. 157, 24–40.
Duprat, L.P.A.M., Bigg, G.R., Wilton, D.J., 2016. Enhanced Southern Ocean marine productivity due to fertilization by giant icebergs. Nat. Geosci. 9 (3), 219–221. https://doi.org/10.1038/ngeo2633.
Fitzsimmons, J.N., Boyle, E.A., 2012. An intercalibration between the GEOTRACES GO-FLO and the MITESS/Vanes sampling systems for dissolved iron concentration analyses (and a closer look at adsorption effects). Limnol. Oceanogr. Methods 10 (6), 437–450.
Fitzsimmons, J.N., John, S.G., Marsay, C.M., Hoffman, C.L., Nicholas, S.L., Toner, B.M., German, C.R., Sherrell, R.M., 2017. Iron persistence in a distal hydrothermal plume supported by dissolved–particulate exchange. Nat. Geosci. 10 (3), 195–201.
Frölicher, T.L., Sarmiento, J.L., Paynter, D.J., Dunne, J.P., Krasting, J.P., Winton, M., 2015. Dominance of the Southern Ocean in anthropogenic carbon and heat uptake in CMIP5 models. J. Clim. 28 (2), 862–886.
Gerringa, L.J.A., et al., 2014. A critical look at the calculation of the binding characteristics and concentration of iron complexing ligands in seawater with suggested improvements. Environ. Chem. 11 (2), 114–136.
Gerringa, L.J., Alderkamp, A.-C., Laan, P., Thuroczy, C.-E., De Baar, H.J., Mills, M.M., van Dijken, G.L., van Haren, H., Arrigo, K.R., 2012. Iron from melting glaciers fuels the phytoplankton blooms in Amundsen Sea (Southern Ocean): Iron biogeochemistry. Deep-Sea Res. II Top. Stud. Oceanogr. 71, 16–31.
Gerringa, L.J.A., Laan, P., van Dijken, G.L., van Haren, H., De Baar, H.J.W., Arrigo, K.R., Alderkamp, A.-C., 2015. Sources of iron in the Ross Sea polynya in early summer. Mar. Chem. 177, 447–459. https://doi.org/10.1016/j.marchem.2015.06.002.
Gerringa, L.J.A., Slagter, H.A., Bown, J., van Haren, H., Laan, P., De Baar, H.J.W., Rijkenberg, M.J.A., 2017. Dissolved Fe and Fe-binding organic ligands in the Mediterranean Sea–GEOTRACES G04. Mar. Chem. 194, 100–113.
Gerringa, L.J.A., Alderkamp, A.-C., Laan, P., Thuróczy, C.-E., de Baar, H.J.W., Mills, M.M., van Dijken, G.L., van Haren, H., Arrigo, K.R., 2020. Corrigendum to“ Iron from melting glaciers fuels the phytoplankton blooms in Amundsen Sea (Southern Ocean): Iron biogeochemistry”(Gerringa et al., 2012). Deep-Sea Res. II Top. Stud. Oceanogr. 177, 104843.
Gerringa, L.J., Gledhill, M., Ardiningsih, I., Muntjewerf, N., Laglera, L.M., 2021. Comparing CLE-AdCSV applications using SA and TAC to determine the Fe binding characteristics of model ligands in seawater. Biogeosci. Discuss. 1–40.
Gledhill, M., Buck, K., 2012. The organic complexation of iron in the marine environment: a review. Front. Microbiol. 3. https://www.frontiersin.org/articles/10.3389/fmicb.2012.00069.
Goldberg, E.D., 1954. Marine geochemistry 1. Chemical scavengers of the sea. J. Geol. 62 (3), 249–265.
Gordon, L.I., Jennings Jr., J.C., Ross, A.A., Krest, J.M., 1993. A suggested protocol for continuous flow automated analysis of seawater nutrients (phosphate, nitrate, nitrite and silicic acid) in the WOCE Hydrographic Program and the Joint Global Ocean Fluxes Study. In: WOCE Hydrographic Program Office, Methods Manual WHPO, 68/91, pp. 1–52.
Gustafsson, J.P., 2012. Visual Minteq, a Free Equilibrium Speciation Model. KTH, Department of Land and Water Resources Engineering.
Hatta, M., Measures, C.I., Lam, P.J., Ohnemus, D.C., Auro, M.E., Grand, M.M., Selph, K.E., 2017. The relative roles of modified circumpolar deep water and benthic sources in supplying iron to the recurrent phytoplankton blooms above Pennell and Mawson banks, Ross Sea, Antarctica. J. Mar. Syst. 166, 61–72. https://doi.org/10.1016/j.jmarsys.2016.07.009.
Hopwood, M.J., Cantoni, C., Clarke, J.S., Cozzi, S., Achterberg, E.P., 2017. The heterogeneous nature of Fe delivery from melting icebergs. Geochem. Perspect. Lett. 3, 200–209.
Hu, Z., Gao, S., 2008. Upper crustal abundances of trace elements: a revision and update. Chem. Geol. 253 (3), 205–221. https://doi.org/10.1016/j.chemgeo.2008.05.010.
Hurst, M.P., Aguilar-Islas, A.M., Bruland, K.W., 2010. Iron in the southeastern Bering Sea: elevated leachable particulate Fe in shelf bottom waters as an important source for surface waters. Cont. Shelf Res. 30 (5), 467–480.
Janssens, J., Meiners, K.M., Tison, J.-L., Dieckmann, G., Delille, B., Lannuzel, D., 2016. Incorporation of iron and organic matter into young Antarctic Sea ice during its initial growth stages. Elementa 4 (000123). https://doi.org/10.12952/journal.elementa.000123.
Jeon, M.H., Jung, J., Park, M.O., Aoki, S., Kim, T.-W., Kim, S.-K., 2021. Tracing circumpolar deep water and glacial meltwater using humic-like fluorescent dissolved organic matter in the Amundsen Sea, Antarctica. Mar. Chem. 235, 104008.
Khatiwala, S., Primeau, F., Hall, T., 2009. Reconstruction of the history of anthropogenic CO 2 concentrations in the ocean. Nature 462 (7271), 346–349.
King, A.L., Sañudo-Wilhelmy, S.A., Boyd, P.W., Twining, B.S., Wilhelm, S.W., Breene, C., Ellwood, M.J., Hutchins, D.A., 2012. A comparison of biogenic iron quotas during a diatom spring bloom using multiple approaches. Biogeosciences 9 (2), 667–687. https://doi.org/10.5194/bg-9-667-2012.
Kwon, Y.S., La, H.S., Jung, J., Lee, S.H., Kim, T.-W., Kang, H.-W., Lee, S., 2021. Exploring the roles of iron and irradiance in dynamics of diatoms and Phaeocystis in the Amundsen Sea continental shelf water. J. Geophys. Res. Oceans 126 (3) (e2020JC016673).
Laglera, L.M., Tovar-Sánchez, A., Iversen, M.H., González, H.E., Naik, H., Mangesh, G., Assmy, P., Klaas, C., Mazzocchi, M.G., Montresor, M., Naqvi, S.W.A., Smetacek, V., Wolf-Gladrow, D.A., 2017. Iron partitioning during LOHAFEX: copepod grazing as a major driver for iron recycling in the Southern Ocean. Mar. Chem. 196, 148–161. https://doi.org/10.1016/j.marchem.2017.08.011.
Landing, W.M., Bruland, K.W., 1987. The contrasting biogeochemistry of iron and manganese in the Pacific Ocean. Geochim. Cosmochim. Acta 51 (1), 29–43.
Lannuzel, D., Schoemann, V., De Jong, J., Pasquer, B., Van der Merwe, P., Masson, F., Tison, J.-L., Bowie, A., 2010. Distribution of dissolved iron in Antarctic Sea ice: spatial, seasonal, and inter-annual variability. J. Geophys. Res. Biogeosci. 115 (G3).
Lannuzel, D., van der Merwe, P.C., Townsend, A.T., Bowie, A.R., 2014. Size fractionation of iron, manganese and aluminium in Antarctic fast ice reveals a lithogenic origin and low iron solubility. Mar. Chem. 161, 47–56. https://doi.org/10.1016/j.marchem.2014.02.006.
Lannuzel, D., Grotti, M., Abelmoschi, M.L., Van Der Merwe, P., 2015. Organic ligands control the concentrations of dissolved iron in Antarctic Sea ice. Mar. Chem. 174, 120–130.
Latour, P., Wuttig, K., van der Merwe, P., Strzepek, R.F., Gault-Ringold, M., Townsend, A.T., Holmes, T.M., Corkill, M., Bowie, A.R., 2021. Manganese biogeochemistry in the Southern Ocean, from Tasmania to Antarctica. Limnol. Oceanogr. https://doi.org/10.1002/lno.11772 n/a(n/a).
Lin, H., Rauschenberg, S., Hexel, C.R., Shaw, T.J., Twining, B.S., 2011. Free-drifting icebergs as sources of iron to the Weddell Sea. Deep-Sea Res. II Top. Stud. Oceanogr. 58 (11–12), 1392–1406.
Meredith, M.P., Venables, H.J., Clarke, A., Ducklow, H.W., Erickson, M., Leng, M.J., Lenaerts, J.T., van den Broeke, M.R., 2013. The freshwater system west of the Antarctic peninsula: spatial and temporal changes. J. Clim. 26 (5), 1669–1684.
Middag, R., de Baar, H.J.W., Laan, P., Cai, P.H., van Ooijen, J.C., 2011. Dissolved manganese in the Atlantic sector of the Southern Ocean. Deep-Sea Res. II Top. Stud. Oceanogr. 58 (25–26), 2661–2677. https://doi.org/10.1016/j.dsr2.2010.10.043.
Middag, R., Séférian, R., Conway, T.M., John, S.G., Bruland, K.W., de Baar, H.J., 2015. Intercomparison of dissolved trace elements at the Bermuda Atlantic time series station. Mar. Chem. 177, 476–489.
Miles, T., Lee, S.H., Waahlin, A., Ha, H.K., Kim, T.W., Assmann, K.M., Schofield, O., 2016. Glider observations of the Dotson ice shelf outflow. Deep-Sea Res. II Top. Stud. Oceanogr. 123, 16–29.
Milne, A., Schlosser, C., Wake, B.D., Achterberg, E.P., Chance, R., Baker, A.R., Forryan, A., Lohan, M.C., 2017. Particulate phases are key in controlling dissolved iron concentrations in the (sub) tropical North Atlantic. Geophys. Res. Lett. 44 (5), 2377–2387.
Nakamura, K., Aoki, S., Yoshimura, K., Kurita, N., 2014. Distribution of oxygen isotope ratio of precipitation in the Atlantic-Indian sectors of the Southern Ocean. Sola 10, 154–157.
Nitsche, F.O., Jacobs, S.S., Larter, R.D., Gohl, K., 2007. Bathymetry of the Amundsen Sea continental shelf: implications for geology, oceanography, and glaciology. Geochem. Geophys. Geosyst. 8 (10).
Ohnemus, D.C., Lam, P.J., 2015. Cycling of lithogenic marine particles in the US GEOTRACES North Atlantic transect. Deep-Sea Res. II Top. Stud. Oceanogr. 116, 283–302.
Ohnemus, D.C., Auro, M.E., Sherrell, R.M., Lagerström, M., Morton, P.L., Twining, B.S., Rauschenberg, S., Lam, P.J., 2014. Laboratory intercomparison of marine particulate digestions including piranha: a novel chemical method for dissolution of polyethersulfone filters. Limnol. Oceanogr. Methods 12 (8), 530–547.
Oliver, H., St-Laurent, P., Sherrell, R.M., Yager, P.L., 2019. Modeling iron and light controls on the summer Phaeocystis antarctica bloom in the Amundsen Sea polynya. Glob. Biogeochem. Cycles 33 (5), 570–596.
Östlund, H.G., Hut, G., 1984. Arctic Ocean water mass balance from isotope data. J. Geophys. Res. Oceans 89 (C4), 6373–6381.
Park, J., Kuzminov, F.I., Bailleul, B., Yang, E.J., Lee, S., Falkowski, P.G., Gorbunov, M.Y., 2017. Light availability rather than Fe controls the magnitude of massive phytoplankton bloom in the Amundsen Sea polynyas, Antarctica. Limnol. Oceanogr. 62 (5), 2260–2276.
Pausch, F., Bischof, K., Trimborn, S., 2019. Iron and manganese co-limit growth of the Southern Ocean diatom Chaetoceros debilis. PLoS One 14 (9), e0221959.
Peers, G., Price, N.M., 2004. A role for manganese in superoxide dismutases and growth of iron-deficient diatoms. Limnol. Oceanogr. 49 (5), 1774–1783.
Planquette, H., Sherrell, R.M., 2012. Sampling for particulate trace element determination using water sampling bottles: methodology and comparison to in situ pumps. Limnol. Oceanogr. Methods 10 (5), 367–388.

Planquette, H., Sherrell, R.M., Stammerjohn, S., Field, M.P., 2013. Particulate iron delivery to the water column of the Amundsen Sea, Antarctica. Mar. Chem. 153, 15–30.
Poulton, S.W., Canfield, D.E., 2005. Development of a sequential extraction procedure for iron: implications for iron partitioning in continentally derived particulates. Chem. Geol. 214 (3), 209–221. https://doi.org/10.1016/j.chemgeo.2004.09.003.
Randall-Goodwin, E., Meredith, M.P., Jenkins, A., Yager, P.L., Sherrell, R.M., Abrahamsen, E.P., Guerrero, R., Yuan, X., Mortlock, R.A., Gavahan, K., 2015. Freshwater distributions and water mass structure in the Amundsen Sea Polynya region, Antarctica. Elementa 3.
Raven, J.A., 2013. Iron acquisition and allocation in stramenopile algae. J. Exp. Bot. 64 (8), 2119–2127.
Raven, J.A., Falkowski, P.G., 1999. Oceanic sinks for atmospheric CO $_2$. Plant Cell Environ. 22 (6), 741–755. https://doi.org/10.1046/j.1365-3040.1999.00419.x.
Rijkenberg, M.J., de Baar, H.J., Bakker, K., Gerringa, L.J., Keijzer, E., Laan, M., Laan, P., Middag, R., Ober, S., van Ooijen, J., 2015. "PRISTINE", a new high volume sampler for ultraclean sampling of trace metals and isotopes. Mar. Chem. 177, 501–509.
Rintoul, S.R., 2018. The global influence of localized dynamics in the Southern Ocean. Nature 558 (7709), 209–218. https://doi.org/10.1038/s41586-018-0182-3.
Schlitzer, R., 2021. Ocean Data View. https://odv.awi.de.
Schofield, O., Miles, T., Alderkamp, A.-C., Lee, S., Haskins, C., Rogalsky, E., Sipler, R., Sherrell, R.M., Yager, P.L., Tremblay, J.-É., 2015. In situ phytoplankton distributions in the Amundsen Sea Polynya measured by autonomous glidersPhytoplankton in the Amundsen Sea Polynya. Elementa 3.
Sedwick, P.N., Bowie, A.R., Trull, T.W., 2008. Dissolved iron in the Australian sector of the Southern Ocean (CLIVAR SR3 section): meridional and seasonal trends. Deep-Sea Res. I Oceanogr. Res. Pap. 55 (8), 911–925.
Seyitmuhammedov, K., Stirling, C.H., Reid, M.R., van Hale, R., Laan, P., Arrigo, K.R., van Dijken, G., Alderkamp, A.-C., Middag, R., 2021. The distribution of Fe across the shelf of the Western Antarctic peninsula at the start of the phytoplankton growing season. Mar. Chem. 104066.
Shaked, Y., Lis, H., 2012. Disassembling Iron availability to phytoplankton. Front. Microbiol. 3, 123. https://doi.org/10.3389/fmicb.2012.00123.
Sherrell, R.M., Lagerström, M.E., Forsch, K.O., Stammerjohn, S.E., Yager, P.L., 2015. Dynamics of Dissolved iron and Other Bioactive Trace Metals (Mn, Ni, Cu, Zn) in the Amundsen Sea Polynya.
Sherrell, R.M., Annett, A.L., Fitzsimmons, J.N., Roccanova, V.J., Meredith, M.P., 2018. A 'shallow bathtub ring' of local sedimentary iron input maintains the palmer deep biological hotspot on the West Antarctic peninsula shelf. Philos. Trans. R. Soc. A Math. Phys. Eng. Sci. 376 (2122), 20170171. https://doi.org/10.1098/rsta.2017.0171.
Sieber, M., Conway, T.M., de Souza, G.F., Hassler, C.S., Ellwood, M.J., Vance, D., 2021. Isotopic fingerprinting of biogeochemical processes and iron sources in the iron-limited surface Southern Ocean. Earth Planet. Sci. Lett. 567, Scopus. https://doi.org/10.1016/j.epsl.2021.116967.
Silvano, A., Rintoul, S.R., Peña-Molino, B., Hobbs, W.R., van Wijk, E., Aoki, S., Tamura, T., Williams, G.D., 2018. Freshening by glacial meltwater enhances melting of ice shelves and reduces formation of Antarctic bottom water. Sci. Adv. 4 (4), eaap9467. https://doi.org/10.1126/sciadv.aap9467.
Slagter, H.A., Reader, H.E., Rijkenberg, M.J.A., Van Der Loeff, M.R., De Baar, H.J.W., Gerringa, L.J.A., 2017. Organic Fe speciation in the Eurasian basins of the Arctic Ocean and its relation to terrestrial DOM. Mar. Chem. 197, 11–25.
Smith, K.L., Robison, B.H., Helly, J.J., Kaufmann, R.S., Ruhl, H.A., Shaw, T.J., Twining, B.S., Vernet, M., 2007. Free-drifting icebergs: hot spots of chemical and biological enrichment in the Weddell Sea. Science 317 (5837), 478–482.
St-Laurent, P., Yager, P.L., Sherrell, R.M., Stammerjohn, S.E., Dinniman, M.S., 2017. Pathways and supply of dissolved iron in the Amundsen Sea (Antarctica). J. Geophys. Res. Oceans 122 (9), 7135–7162. https://doi.org/10.1002/2017JC013162.
St-Laurent, P., Yager, P.L., Sherrell, R.M., Oliver, H., Dinniman, M.S., Stammerjohn, S.E., 2019. Modeling the seasonal cycle of iron and carbon fluxes in the Amundsen Sea polynya, Antarctica. J. Geophys. Res. Oceans 124 (3), 1544–1565. https://doi.org/10.1029/2018JC014773.
Strzepek, R.F., Boyd, P.W., Sunda, W.G., 2019. Photosynthetic adaptation to low iron, light, and temperature in Southern Ocean phytoplankton. Proc. Natl. Acad. Sci. 116 (10), 4388–4393. https://doi.org/10.1073/pnas.1810886116.
Sunda, W.G., Huntsman, S.A., 1995. Iron uptake and growth limitation in oceanic and coastal phytoplankton. Mar. Chem. 50 (1–4), 189–206.
Sunda, W.G., Huntsman, S.A., Harvey, G.R., 1983. Photoreduction of manganese oxides in seawater and its geochemical and biological implications. Nature 301 (5897), 234–236.
Tagliabue, A., Mtshali, T., Aumont, O., Bowie, A.R., Klunder, M.B., Roychoudhury, A.N., Swart, S., 2012. A global compilation of dissolved iron measurements: focus on distributions and processes in the Southern Ocean. Biogeosciences 9 (6), 2333–2349.
Taylor, S.R., McLennan, S.M., 1985. The Continental Crust: Its Composition and Evolution.
Taylor, S.R., McLennan, S.M., 1995. The geochemical evolution of the continental crust. Rev. Geophys. 33 (2), 241–265.
Thuróczy, C.-E., Alderkamp, A.-C., Laan, P., Gerringa, L.J., Mills, M.M., Van Dijken, G.L., De Baar, H.J., Arrigo, K.R., 2012. Key role of organic complexation of iron in sustaining phytoplankton blooms in the Pine Island and Amundsen polynyas (Southern Ocean). Deep-Sea Res. II Top. Stud. Oceanogr. 71, 49–60.
Tian, H., van Manen, M., Wille, F., Jung, J., Lee, S.H., Kim, T.W., Aoki, S., Eich, C., Brussaard, C.P.D., Reichart, G., Conway, T., Middag, R., 2022. The biogeochemistry of zinc and cadmium in the Amundsen Sea, coastal Antarctica. Mar. Chem. (In Review).
Tortell, P.D., Maldonado, M.T., Price, N.M., 1996. The role of heterotrophic bacteria in iron-limited ocean ecosystems. Nature 383 (6598), 330–332.
Turekian, K.K., 1977. The fate of metals in the oceans. Geochim. Cosmochim. Acta 41 (8), 1139–1144.
Twining, B.S., Baines, S.B., 2013. The trace metal composition of marine phytoplankton. Annu. Rev. Mar. Sci. 5, 191–215.
Twining, B.S., Baines, S.B., Fisher, N.S., 2004. Element stoichiometries of individual plankton cells collected during the Southern Ocean Iron experiment (SOFeX). Limnol. Oceanogr. 49 (6), 2115–2128.
Twining, B.S., Rauschenberg, S., Morton, P.L., Vogt, S., 2015. Metal contents of phytoplankton and labile particulate material in the North Atlantic Ocean. Prog. Oceanogr. 137, 261–283.
Twining, B.S., Antipova, O., Chappell, P.D., Cohen, N.R., Jacquot, J.E., Mann, E.L., Marchetti, A., Ohnemus, D.C., Rauschenberg, S., Tagliabue, A., 2021. Taxonomic and nutrient controls on phytoplankton iron quotas in the ocean. Limnol. Oceanogr. Lett. 6 (2), 96–106.
Van Heukelem, L., Thomas, C.S., 2001. Computer-assisted high-performance liquid chromatography method development with applications to the isolation and analysis of phytoplankton pigments. J. Chromatogr. A 910 (1), 31–49.
Van Leeuwe, M.A., Villerius, L.A., Roggeveld, J., Visser, R.J.W., Stefels, J., 2006. An optimized method for automated analysis of algal pigments by HPLC. Mar. Chem. 102 (3–4), 267–275.
Wagener, T., Guieu, C., Losno, R., Bonnet, S., Mahowald, N., 2008. Revisiting atmospheric dust export to the southern Hemisphere Ocean: biogeochemical implications. Glob. Biogeochem. Cycles 22 (2).
Wehrmann, L.M., Formolo, M.J., Owens, J.D., Raiswell, R., Ferdelman, T.G., Riedinger, N., Lyons, T.W., 2014. Iron and manganese speciation and cycling in glacially influenced high-latitude fjord sediments (West Spitsbergen, Svalbard): evidence for a benthic recycling-transport mechanism. Geochim. Cosmochim. Acta 141, 628–655. https://doi.org/10.1016/j.gca.2014.06.007.
Wu, M., McCain, J.S.P., Rowland, E., Middag, R., Sandgren, M., Allen, A.E., Bertrand, E. M., 2019. Manganese and iron deficiency in Southern Ocean Phaeocystis antarctica populations revealed through taxon-specific protein indicators. Nat. Commun. 10 (1), 3582. https://doi.org/10.1038/s41467-019-11426-z.
Yager, P.L., Sherrell, R.M., Stammerjohn, S.E., Alderkamp, A.-C., Schofield, O., Abrahamsen, E.P., Arrigo, K.R., Bertilsson, S., Garay, D.L., Guerrero, R., 2012. ASPIRE: the Amundsen Sea polynya international research expedition. Oceanography 25 (3), 40–53.